

COMPUTATIONAL MODELING & SCALING
OF PLUME INDUCED FLOW SEPARATION

by

YITONG GAO

JOHN BAKER, COMMITTEE CHAIR

CLARK MIDKIFF
PAUL RAY
WILLARD SCHREIBER
STEVE KAVANAUGH

A Dissertation

Submitted in partial fulfillment of the requirements
for the degree of Doctor of Philosophy
in the Department of Mechanical Engineering
in the Graduate School of
The University of Alabama

TUSCALOOSA, ALABAMA

2014

ABSTRACT

This dissertation investigated the flow behavior of converging-diverging nozzle numerically. Results of a study exploring the use of saw-tooth surface modifications to improve supersonic micronozzle performance are presented. For certain configurations, the saw-tooth wall modification considered in this study produced an effective “velocity slip” along the surface of the nozzle, thus reducing the influence of viscous forces and enhancing nozzle performance. A parametric study examined how variations in the geometric scale and configuration of the individual “saw teeth” affected flow behavior, specific impulse, and thrust coefficient. By increasing the number of saw teeth, a point was reached where viscous forces damped out the impact that the surface modifications had on the overall flow field behavior. Under certain conditions, the saw-tooth surface modification was shown to increase nozzle performance.

The flow structure of the exhaust from a converging-diverging nozzle into supersonic flow field has been investigated for both steady-state and transient analyses. The results of this study are presented, with particular emphasis on plume induced flow separation. The CD nozzles with straight afterbody configurations, having throat diameters on $\mathcal{O}(10^{-3}\text{m})$ to $\mathcal{O}(10^{-2}\text{m})$ were examined. The parametric studies involving freestream Mach number (Ma_∞), chamber-to-ambient pressure ratio (P_c/P_∞) and the geometric scaling effects was conducted to explore the impact these parameters had on base-flow/plume interactions and plume induced flow separation (PIFS). The plume induced shockwave motion as well as the “hot zone” caused by the base-flow/plume interaction were investigated by considering Ma_∞ and P_c/P_∞ . The 2-equation $k - \epsilon$ Re-Normalization Group (RNG) model and $k - \omega$ Shear Stress Transportation (SST) model

were utilized for turbulence calculation. Grid independent computational models were validated by comparison with previously published data. Correlations showing the relation between the boundaries of the recirculation zone when PIFS is present as well as the plume induced shock motion with respect to Ma_∞ and P_c/P_∞ are presented. Values of these parameters when PIFS and base-flow/plume interaction occur are discussed as a function of geometry.

DEDICATION

This dissertation is dedicated to everyone who helped me and guided me through the trials and tribulations of creating this manuscript. In particular, my family and close friends who stood by me throughout the time taken to complete this masterpiece.

LIST OF ABBREVIATIONS AND SYMBOLS

1D	1D isentropic relation
A_{throat}	nozzle throat area
A_{exit}	nozzle exit area
A_{viscous}	viscous region
C_D	discharge coefficient
C_f	thrust coefficient
D_t	throat diameter
E	total energy
F_t	thrust
I_{sp}	specific impulse
$I_{\text{sp, inviscid}}$	specific impulse of inviscid case
Kn	Knudsen number
L	nozzle length
Ma	Mach number
N	number of saw teeth
P_b	back pressure
P	static pressure
P_e	exit pressure
P_o	stagnation pressure
P_{out}	outlet pressure

P_{total}	total pressure
P_{in}	inlet pressure
P_{op}	operating pressure
PR	chamber-to-ambient pressure ratio
R	universal gas constant
Re	Reynolds number
Re_t	nozzle throat Reynolds number
R_t	nozzle throat radius
T	static temperature
T_o	stagnation temperature
T_{in}	inlet temperature
\mathbf{V}	velocity vector
r	nozzle radius
y	geometric characteristic length
v_{cl}	centerline velocity
g_o	gravitational acceleration
h	enthalpy
k	turbulent kinetic energy
l	characteristic length
\dot{m}	mass flow rate
u_e	exit velocity
α	angle of saw teeth
κ	thermal conductivity
γ	specific heat ratio
ε	expansion area ratio

η	percentage performance increase
θ	divergent half-angle
λ	mean free path
ρ	working fluid density
τ	viscous shear tensor
μ	fluid viscosity
μ_t	turbulent viscosity
ϵ	specific dissipation
δ_{exit}	exit plane boundary layer
∞	freestream state
c	nozzle chamber state

ACKNOWLEDGMENTS

I would first like to thank the University of Alabama Mechanical Engineering Department for providing the support for my project. I would also like to thank Dr. John Baker for his patience, guidance, and persistence during my studies and research project. I would like to thank Dr. Clark Midkiff, Dr. Paul Ray, Dr. Willard Schreiber and Dr. Steve Kavanaugh for being my committee members and providing me direction on my research. I would also like to thank Mrs. Betsy Singleton for her valuable insight during my study. I would also like to thank my family and friends for their continuous support and encouragement. Most importantly, I give all the praise and thanks to my savior Jesus Christ, who gives me courage and leads me through the days in the United States of America.

CONTENTS

ABSTRACT.....	ii
DEDICATION.....	iv
LIST OF ABBREVIATIONS AND SYMBOLS	v
ACKNOWLEDGMENTS	viii
LIST OF TABLES.....	xii
LIST OF FIGURES	xiii
1. INTRODUCTION	1
1.1 Background of Converging-Diverging Nozzle.....	1
1.2 Introduction to Small-Scale Converging-Diverging nozzle	2
1.3 Statistical Numerical Method applied on Rarefied Flow.....	6
1.4 Introduction of Plume Induced Flow Separation (PIFS)	10
1.5 Thermal Radiation Effects on Plume Induced Flow Interaction	13
1.6 Objectives and Dissertation Organization	14
2. PERFORMANACE IMPROVEMENT VIA INTERNAL SURFACE MODIFICATIONS OF SUPERSONIC MICRONOZZLES.....	15
2.1 Significance of Viscous Effects on Microscale Converging-Diverging Nozzle	15

2.1.1 Mathematical Formulation.....	15
2.1.2 Numerical Method	17
2.1.3 Verification & Validation	18
2.1.4 No-Slip Boundary Condition: Justification	20
2.1.5 Internal Converging-Diverging Nozzle Flow: Viscous Effects.....	21
2.2 “Saw Tooth” Surface Modification	28
2.2.1 Justification of No-Slip Boundary Condition for “Saw Tooth” Modification.....	29
2.2.2 “Saw Tooth” Surface Modification Flow Illustration.....	30
2.2.3 Performance of “Saw Tooth Surface Modification on Micronozzle”	31
3. COMPUTATIONAL INVESTIGATION OF SCALING EFFECTS ON PLUME INDUCED FLOW SEPARATION (PIFS)	36
3.1 Computational Schematic and Mathematical Formulation.....	36
3.1.1 Numerical Method	38
3.1.2 Verification & Validation	40
3.2 Results & Discussion	41
3.2.1 Effects of Pressure Ratio (PR) on Plume Induced Flow Separation (PIFS)	41
3.2.2 Effects of Freestream Flow (Ma_∞) on Plume Induced Flow Separation (PIFS)	45
3.2.3 Effects of Geometry Scaling (Re_∞) on Plume Induced Flow Separation (PIFS)	51
4. TRANSIENT ANALYSIS OF PLUME INDUCED SHOCKWAVE AND PLUME INDUCED FLOW SEPARATION ON MINIATURIZED CD NOZZLE.....	55
4.1 Computational Schematic and Mathematical Formulation.....	55
4.1.1 Numerical Method	57
4.1.2 Verification & Validation	58
4.2 Results & Discussion	59

4.2.1 Effects of Pressure Ratio (PR) on Plume Induced Shockwave and PIFS	59
4.2.2 Effects of Freestream Flow (Ma_∞) on Plume Induced Shockwave and PIFS	66
5. CONCLUSIONS.....	73
5.1 Conclusions of “Saw Tooth” Surface Modification on Microscale CD Nozzle.....	73
5.2 Conclusions on the Analysis of PIFS on CD Nozzle	74
5.3 Conclusions on the Transient Analysis of CD Nozzle.....	76
6. REFERENCES	78

LIST OF TABLES

Table 1 Baseline parameters used to generate computational results.....	20
Table 2 Values of throat radius considered.....	20
Table 3 Baseline parameters considered for the Pressure Ratio (PR) effect	41
Table 4 Baseline parameters considered for the Freestream Mach (Ma_∞) effect	46
Table 5 Baseline parameters considered for the Geometry Scaling (Re_∞) effect	51
Table 6 Baseline parameters considered for the Pressure Ratio (PR) effect	59
Table 7 Baseline parameters considered for the Freestream Mach (Ma_∞) effect	66

LIST OF FIGURES

Fig.1 A schematic diagram of the microscale CD nozzle without surface modification ..	16
Fig.2 A domain highlighting the structure of typical grid in the micronozzle	17
Fig.3 Validation of computational model	19
Fig.4 Kn contour for case 5 ($R_t = 30 \mu m$)	21
Fig.5 Mach contour for case 1 ($R_t = 80 \mu m$) to case 5 ($R_t = 30 \mu m$)	23
Fig.6 Pressure and temperature ratio along the nozzle centerline	25
Fig.7 Discharge coefficient (C_f) for $R_t = 30 \mu m$ to $R_t = 80 \mu m$	26
Fig.8 Specific impulse efficiency ($I_{sp}/I_{sp,invicid}$) for $R_t = 30 \mu m$ to $R_t = 80 \mu m$	27
Fig.9 Viscous region ratios for $R_t = 30 \mu m$ to $R_t = 80 \mu m$	28
Fig.10 “Saw Tooth” nozzle wall configuration	29
Fig.11 Kn contour for $N=60$	29
Fig.12 Flow conditions illustrations for two types of nozzle wall.....	30
Fig.13 Streamline neat the wall for $N=40$	31
Fig.14 Mach contour for $N=60$	32
Fig.15 Thrust coefficient (C_f) for $N=0$ to $N=60$	33
Fig.16 Specific impulse efficiency ($I_{sp}/I_{sp,invicid}$) for $N=0$ to $N=60$	33
Fig.17 Thrust coefficient (C_f) for $N=60$ from $\alpha = 15^\circ$ to $\alpha = 30^\circ$	34
Fig.18 Specific impulse efficiency for $N=60$ from $\alpha = 15^\circ$ to $\alpha = 30^\circ$	35
Fig.19 PIFS phenomena on a straight afterbody configuration	37

Fig.20 Computational domain	39
Fig.21 Validation of computational model	40
Fig.22 Pressure ratio effects on PIFS and Base-Flow/Plume Interaction.....	42
Fig.23 Base-flow separation locations along the Base-Surface.....	44
Fig.24 Heat Flux distribution along Base-Surface.....	45
Fig.25 Freestream flow condition effect on PIFS and Base-Flow/Plume Interaction	47
Fig.26 Freestream effects on heat flux distribution along the Base-Surface	49
Fig.27 Freestream effects on PIFS locations along the Upper-Surface	50
Fig.28 Geometry Scaling (Re_∞) Effects on Base-Flow/Plume Interaction	52
Fig.29 Geometry Scaling Effects on Heat Flux Distribution along the Base-Surface	53
Fig.30 Plume-Freestream interference schematic.....	56
Fig.31 Computational domain	58
Fig.32 Validation of computational model	59
Fig.33 P_c/P_∞ pressure ratio effects on plume induced shockwave.....	60
Fig.34 Plume induced shockwave locations affected by P_c/P_∞ pressure ratio.....	62
Fig.35 PIFS phenomenon affected by P_c/P_∞ pressure ratio	63
Fig.36 Motion of “Hot Zone” along the Base-Surface affected by P_c/P_∞ pressure ratio	65
Fig.37 Freestream Mach number effects on plume induced shockwave	66
Fig.38 Plume induced shockwave locations affected by freestream Mach number	69
Fig.39 Base-Surface/Plume interaction affected by the freestream Mach number	70
Fig.40 “Hot Zone” along the Base-Surface affected by the freestream Mach number	71

CHAPTER 1

INTRODUCTION

This chapter provides a general background of the field of microscale, small-scale converging-diverging nozzle and miniaturized flight vehicle. A brief overview of certain specific aspects of the study is also provided.

1.1 Background of Converging-Diverging Nozzle

The converging-diverging nozzle, also referred as de Laval nozzle, was first developed by Gustaf de Laval [1] [2] in 1888 for the use on steam turbine, which consisted of a tube “pinched” in the middle, asymmetric hourglass-shape and can be used to accelerate pressurized gas to supersonic speed by passing through. Because of this, de Laval nozzle is often used in steam turbines and also used as rocket engine nozzle. The de Laval nozzle was first used in the early rocket engine developed by Robert Gaddard [3], since then it has been widely used in almost all the rocket engines. The supersonic compressible flow passing through the nozzle has already been investigated. The one-dimensional isentropic expansion analysis generally agrees with the experimental data [4] [5] for high Reynolds numbers ($Re > 10^4$) due to the fact the viscous effects are less than 1% [6].

With the development of small-scale spacecraft technology, the small-scale de Laval nozzle has been investigated and used in the cold gas thruster, which requires high degree of reliability, low system complexity, no combustion involved and low velocity differences. The cold gas thrust refers to a high-pressure propellant at temperatures between 200K and 300K with a low specific impulse, from 40 to 120 seconds [7]. Because of the simplicity and reliability, the

cold gas thrusters are mostly useful for small engines, such as micropropulsion system which can be used on small-scale spacecraft for attitude control [8]. Due to the development of microelectromechanical systems (MEMS) technology, there has been an increasing interest in micropropulsion system that can be used on small-scale spacecraft [9]. The classifications of small-scale spacecraft have been proposed by Air Force Research Laboratory (AFRL) [10] into four categories based on the weights: Class I (small spacecraft, weighs from 100 kg to 1000 kg); Class II (microspacecraft weighs from 10 kg to 100 kg); Class III (nanospacecraft, weighs from 1 kg to 10 kg) and Class IV (picospacecraft, weighs less than 0.001 kg). The micropropulsion systems selection is different among different classifications. Micropropulsion systems typically can generate low thrust from 10^{-6} N to 10^{-3} N with the system mass less than 1 kg [11]. Numbers of reports have been published to address the propulsion options for microspacecraft and satellites [12-14]. One of the critical components in micropropulsion system is the micronozzle.

1.2 Introduction to Small-Scale Converging-Diverging Nozzle

The study of small-scale nozzle with low Reynolds number started in the late 1960s when Milligan [15] focused on the discharge coefficients as well as the low thrusts for the nozzles with throat Reynolds numbers varied from 10^2 to 10^6 by using the nozzles on the scale of 10^{-3} m. Massier [16] et al., conducted similar experiment and measured the discharge coefficients with 10° half-divergence angle nozzles with different stagnation pressures and different working fluids. Kuluva [17] et al., also studied the discharge coefficients by considering the low Reynolds number nozzle in the range from 50 to 1000. Rothe [18] experimentally studied the viscous flow in supersonic nozzles with the throat Reynolds number varying from 10^2 to 10^3 . Rothe concluded that when the Reynolds number is greater than 500, a very small inviscid core was

observed; when the Reynolds number is smaller than 300, the flow become fully viscous and no inviscid core is indicated. March [19] et al., and Whalen [20] also performed the experimental investigations on low Reynolds number nozzle flows. Rae [21] used the slender nozzle approximation to determine the flow profiles by focusing on various nozzle cross sections. Driscoll [22] studied the viscous effects in chemical laser nozzles. Driscoll found that the boundary layer had the same order as the nozzle exit dimensions. The flow became fully viscous when the throat Reynolds number is below 1000. Chung [23] et al., investigated the low-density gas in the nozzle by using DSMC and continuum methods. The numerical results were compared with Rothe [18] experimental data and showed good agreement. Chung carried out different numerical analysis when the flow was under continuum, slip, transitional and free molecular regimes. Hussaini [24] et al., investigated the optimization procedure of low Reynolds number rocket nozzle numerically. The CFD-Based optimization procedure by applying the parabolized N-S equation was used to design conical and contoured axisymmetric nozzles. The results showed that the CFD-based optimization procedure achieved better results than those obtained from Rao [25] nozzle design. Kim [26] studied the effects of viscous on the performance of a resistojet nozzle with full N-S code. Three different configurations with 20° and 30° outlet angles were compared. Kim concluded that the 30° half-divergence conical nozzle had the highest specific impulse among the three nozzles. These early studies had a general agreement on the existence and effects of viscous region at low throat Reynolds number. Shimura [27] et al., studied the supersonic flow in a cooled nozzle using a modified SIMPLER algorithm for compressible flow. A 5° half-divergent angle was applied along the downstream of the throat. From this, Shimura concluded that for high backpressure, the flow in the nozzle is separated from the wall surface, and it occurs only on one side of the wall; also, the thermal boundary layer

is thinner for the isothermal cooled wall compared with the adiabatic flow. Zelesnik [28] et al., studied the low Reynolds number nozzle flows by using the DSMC technique. In these cases, the conical-shaped, trumpet-shaped and bell-shaped nozzles were investigated numerically. The results showed the trumpet-shaped nozzle has the highest efficiency with the unheated flow. Liang [29] et al., analyzed the configurations of the low-thrust nozzles for small satellite application. Both Euler and N-S solver were developed for studying the flow fields and corresponding viscous effect. Bayt [30-31] studied the micronozzles performance with a minimum throat width of 18 μm computationally and experimentally. Bayt found that the thrust efficiency experienced a rapid drop when the throat Reynolds number is below 500. Reed [32] et al., addressed the experimental evaluations of cold gas micronozzles. Numbers of rectangular silicon thruster with the throat widths of 350 μm , area ratios varied from 1 to 25 were tested. The experimental results showed that the nozzle efficiency peaked around 65% at Reynolds numbers at approximately 16000. Ivanov [33] et al., investigated the cold gas micronozzle flows numerically with Reynolds number in the range from 130 to 1300. Both CFD and DSMC were used to compare the results when the flow is in continuum region [34], Ivanov found that when decreasing Reynolds number, the viscous losses become larger, resulting in the specific impulse decreased from the throat region through the nozzle exit. Markelov [35-36] et al., analyzed the cold flow in a 3D micronozzle with a 34 μm throat diameter with both N-S equation and DSMC technique. Choudhuri [37] et al., investigated the geometry effects of nozzles with 0.38 mm throat width. The conical, bell and trumpet shaped nozzles were tested experimentally. Choudhuri found that the conical shaped nozzle with 15° half divergence angle had higher thrust and specific impulse when compared to the conical shaped nozzle with 20° half divergence angle as well as trumpet and bell shaped nozzles. Alexeenko [38-43] et al., Ketsdever [44] et al.,

studied micronozzles for cold gas thrusters by using the DSMC technique with both axisymmetric and three-dimensional configurations as well as the experimental analysis. These studies involved low throat Reynolds number ranging from 0.02 to 200. An improvement of specific impulse was achieved through the decreasing of nozzle length and increasing the nozzle half-divergence angle. Louisos [45-48] et al., numerically studied the subsonic boundary layer effects on axisymmetric as well as three-dimensional supersonic micronozzles. Louisos found that there was inherent tradeoff between nozzle thrust and efficiency and the viscous losses, as well as the losses due to the non-axial exit flow at larger half-divergence angle. Louisos also carried out the transient analysis for three-dimensional cases numerically, where the viscous effects were more obvious because of the depth dimension existence in three-dimensional analysis. Titov [49] et al., examined a collision-limiter approach of DSMC technique for micropropulsion system. This approach provided a wider range of DSMC technique for solving the flow from the transitional to continuum regime. Mo [50] et al., studied the gas flow in conical micronozzles by looking at the axisymmetric case with both DSMC technique and continuum methods. Mo concluded that when throat Reynolds number is less than 10, the DSMC technique predicts a larger thrust compared to the continuum method. Lin [51-52] et al., numerically studied the rarefied gas passing through the micronozzle with different throat diameters. Continuum methods with slip and no-slip boundary conditions were studied. The throat diameters varied from 0.1 mm to 10 mm and the throat Reynolds number was in the range from 5 to 2000. Lin concluded that the velocity distribution in the near-wall region showed obvious deviations between slip and no-slip boundary conditions, and the correlation has been derived to predict the specific impulse based on the throat diameter and throat Reynolds number. Ahmad [53] studied the discharge coefficient and heat transfer in a micronozzle. The axisymmetric cases

were considered numerically, different half-convergence angles, stagnation temperatures as well as stagnation pressures were compared. A correlation was derived to describe the discharge coefficient as a function of nozzle convergence half-angle, area ratio and pressure ratio. Most recently, Bruccoleri [54-55] et al., studied supersonic nozzle flow efficiency at low throat Reynolds number experimentally. Bruccoleri suggested that the thrust efficiency was about 80% for a throat Reynolds numbers were above 1500 and was below 60% when the throat Reynolds number reached 400. The wall thickness effects were also investigated, which demonstrated the significance of endwall boundary layer.

1.3 Statistical Numerical Method applied on Rarefied Flow

If a further miniaturized nozzle is being considered, one important parameter to characterize the flow regime, Knudsen number, will increase and the flow will no long be considered as continuum. The Kn was introduced by Brid [34] as in

$$\text{Kn} = \frac{\lambda}{L} \quad (1)$$

For $\text{Kn} < 0.01$, the fluid can be modeled as a continuum; for $0.01 < \text{Kn} < 0.1$, the fluid can be modeled as slip flow; for $0.1 < \text{Kn} < 10$, the fluid can be modeled as transitional flow and for $\text{Kn} > 10$, the fluid can be modeled as free-molecular flow. It is well accepted that when $\text{Kn} < 0.01$, the continuum CFD solver can be applied [56]. For many MEMS devices, the Kn is in the slip or early transitional flow regime. Thus, non-continuum effects could strongly effect on the devices performance [57].

Maxwell [58] first derived the slip relations for dilute, monoatomic gases. The corresponding thermal-creep relation was derived by Smoluchowski [59]. The ideal gas flow with slip wall boundary condition as well as the thermal-creep relation is expressed as

$$U_{\text{slip}} - U_{\text{wall}} = \frac{2-\sigma_v}{\sigma_v} \lambda \left(\frac{\partial u}{\partial y} \right)_w + \frac{3}{4} \frac{\mu}{\rho T_{\text{slip}}} \left(\frac{\partial T}{\partial x} \right)_w \quad (2)$$

$$T_{\text{slip}} - T_{\text{wall}} = \frac{2-\sigma_T}{\sigma_T} \left(\frac{2\gamma}{\gamma+1}\right) \frac{\lambda}{Pr} \left(\frac{\partial T}{\partial y}\right)_w \quad (3)$$

The higher-order slip model and thermal-creep boundary conditions proposed by Karniadakis [60] et al., is given by

$$U_{\text{slip}} - U_{\text{wall}} = \frac{2-\sigma_V}{\sigma_V} \frac{h \cdot K_n}{1-B(K_n) \cdot K_n} \left(\frac{\partial u}{\partial n}\right)_w + \frac{3}{4} \frac{\gamma-1}{\gamma} Pr \frac{\kappa}{\rho R_g T_w} \left(\frac{\partial T}{\partial s}\right)_w + O(K_n^3) \quad (4)$$

$$T_{\text{slip}} - T_{\text{wall}} = \frac{2-\sigma_T}{\sigma_T} \left(\frac{2\gamma}{\gamma+1}\right) \frac{h}{Pr} \frac{K_n}{1-B(K_n) \cdot K_n} \left(\frac{\partial T}{\partial n}\right)_w \quad (5)$$

The DSMC method and continuum method with slip boundary are widely used to study flow field for micro-devices. Piekos [61-62] et al., used DSMC technique to model the flows related to MEMS systems. The optimization was proposed for micro-devices. Nance [63] et al., numerically studied the new DSMC boundary conditions that were suitable for use in low-speed MEMS applications. The new conditions respect the proper directions of signal propagation for subsonic flow and allow specification of inlet and exit pressure. Liou [64] et al., also studied an implicit boundary condition for DSMC technique that can be applied in MEMS flow predictions. The effects of temperatures and geometrics on the performance of MEMS devices were investigated numerically and experimentally [65-66]. Raju [67] et al., studied the micro-thruster with slip boundary condition. The axisymmetric model was developed by using finite element methodology to compare with the 1D isentropic study which was addressed by Rossi [68-69] et al. The results indicated better details of flow inside the micronozzle and gave a more accurate approach of predicting the thrust. Boyd [70-73] et al., analyzed the rarefied gas passing through small-scale nozzle computational and experimental. DSMC technique was used for computational results and the coherent anti-Stokes Raman scattering technique was applied to measure the velocity, translational temperature as well as the thrust of the nozzle at the selected position. We [74] et al., studied the development of two-dimensional DSMC technique to

analyze the micro-scale gas flow with pressure boundary conditions. The micro-manifold, micro-nozzle and slider air bearing were considered as the models. Lockerby [75] et al., considered the fact that for simulations of rarefied flow over curved or moving surfaces, the Maxwell slip boundary condition may be misapplied. Lockerby studied a higher-order slip boundary condition based on the Maxwell general equation and the constitutive relations derived by Burnett. Hao [76] et al., compared the performance of a rectangular cross-section converging-diverging micronozzle with the conventional-shaped micronozzle. The first order of Maxwell slip condition was employed. Hao concluded that there was a closed supersonic area exists in the divergent part of the rectangular cross-section micronozzle instead of a shock wave that usually occurs in the conventional-shaped micronozzle. Xie [77-80] studied the rarefied gas flow with DSMC technique and N-S approach. The numerical results showed that even in continuum region, the DSMC technique shows a better result compared to the experimental data. Li [81] et al., investigated the rarefied gas flow characteristics for different shapes of micro-scale diffusers and nozzles experimentally. Different diffuser/nozzles lengths with different taper angles were designed and fabricated based on silicon micromachining technique. The optimized values for taper angle and the length for the diffuser and nozzles were obtained. Xu [82] et al., analyzed the shock waves inside the micronozzles numerically. N-S solver with slip-wall boundary conditions were imposed for both over-expanded and under-expanded flow conditions. The separation point was observed on the nozzle wall and downstream. The wave interface separated the viscous boundary layer and the inviscid core flow was also observed. The numerical results showed that the viscous effects strongly affect the formation of shock waves in micronozzles. Morinigo [83-85] et al., numerically investigated the slip-model performance for underexpanded micronozzle flows. The second-order slip boundary condition in N-S solver was used. Isothermal and

adiabatic wall, hot and cold gas, as well as the solid-gas heat transfer was analyzed numerically for the underexpanded flow condition. Liu [86] et al., studied the performance of micronozzle flow by using DSMC and continuum method. The results showed that within the Knudsen number range under consideration, both continuum method with slip boundary conditions and DSMC technique shows good agreement except in the nozzle exit lip region, due to the gas rapid expansion. Liu also concluded that with a decreasing stagnation pressure, the difference between continuum model and DSMC started increasing. Within the general agreement than DSMC and continuum method with slip boundary conditions can be applied to small nozzle flows, Broc [87] et al., gained the temperature and density of outer jet flows with laser-induced fluorescence technique and Jamison [88] et al., measured the thrust with and without a divergent part of the nozzle with a throat width of 1 mm.

In response to the relatively high CPU time required to solve for the flow field within the slip regime, the hybrid continuum/practical approach for rarefied flows was developed. Wadsworth [89] et al., Vashchenkov [90] et al., Tiwari [91] et al., studied the 2D hybrid method by applying the hybrid Navier-Stokes simulations with the Chapman-Enskog and Maxwellian distribution. The results showed that the use of Chapman-Enskog distribution will result in a small improvement in accuracy compare to the Maxwellian distribution. Later, Wu [92] et al., developed a coupled DSMC-NS scheme by using the three-dimensional unstructured grid topology. The results showed that the iteratively coupled method predicted a more accurate result compared to the pure DSMC technique or N-S method. Torre [93-94] et al., studied the hybrid method applied on the rarefied supersonic gas flows in micronozzles. It only required 5% – 25% CPU time of full DSMC technique to solve the flow field by applying the hybrid

CFD/DSMC solvers. The proper interface location that separated the CFD and DSMC solvers was determined.

1.4 Introduction of Plume Induced Flow Separation (PIFS)

When a de Laval nozzle is integrated with a launch vehicle or missile body, an increase in the pressure ratio between the nozzle plume and the surrounding atmosphere will happen because of the rapid change in altitude during launching, and the downstream of the exhaust plume will interact with the freestream near the tail of the launch vehicle body. This effect is known as plume induced flow separation (PIFS). Many computational simulations as well as the experiments on PIFS had been studied.

The study of PIFS started at 1960s when McGhee [95-96] studied PIFS of the ballistic bodies at different Mach numbers experimentally. McGhee concluded that due to the PIFS occurring at the base, the launch vehicle experienced a change in aerodynamic force and moment, and also the longitudinal stability is also affected. Walitt [97] et al., studied the PIFS numerically. The laminar flow with Mach number of 26 past a blunt-nosed cone with a spherical after-body which has an orifice diameter of 12 mm was used as the computational model. By varying the Reynolds number of internal flow, Walitt found that for low Reynolds number, the cone and the after-body boundary layers remained attached; for high Reynolds number, the cone and the after-body boundary layers both separated and gave rise to a double-vortex pattern as well as multiple shock waves. Henderson [98] investigated the jet plume effects on missile aerodynamics. The comparisons were made of afterbody pressure distributions affected by plumes of the same shape but with different plume Mach number. Henderson concluded that an increasing of plume Mach number will increase the plume effect on afterbody pressures, and this effect became more pronounced with the increasing of freestream Mach number. Chatelain [99] et al., carried out the

numerical simulation of PIFS on axisymmetric boat-tailed nozzle afterbody configuration. Different turbulent models were used to study the characteristic of PIFS. Ebrahimi [100] et al., studied the three-dimensional effects of the PIFS on the dual-nozzle propulsion system operating at a high-altitude flight condition. The shock reflection location, plume induced shock location and the development of the shear layer region were analyzed numerically and indicated an increase of static temperature, which influenced the entire flow field domain. Bannink [101] et al., studied the underexpanded exhaust plume interaction for a blunted cone-cylinder model rocket numerically and experimentally. The exhausted jet from the nozzle had an exit Mach number of 4 with the supersonic freestream of Mach number 2 and 3. The Euler and Navier-Stokes computations have been performed and compared with the experiments. Matesanz [102] et al., studied the base-flow/plume interaction numerically. The nozzle with a throat diameter of 5 mm was used as the computational model. By given the freestream Mach number 1.96 and varied the pressure ratio from 54 to 397, the base-flow/plume interaction was described with stream pattern of Mach contour, also the flow detachment phenomenon was observed. Raghunathan [103] et al., studied the plume interference effects on missile bodies. The missile configurations with and without the exhaust plume were studied numerically. The freestream Mach number varied from 0.8 to 4.0. Different plume supply pressures from 1.5 atm to 2000 atm were given as the boundary conditions. Raghunathan concluded that for a given freestream Mach number, an increasing plume pressure resulted in an increasing shock strength and upstream movement of the shock on the tail fin; for a given plume pressure ratio, an increasing Mach number resulted in an increase in shock strength and backward motion of the shock on the tail fin. Bakker [104] et al., studied the base flow plume interaction numerically. Different base flow test cases have been selected to validate the code. The boat-tail shaped

afterbody was chosen to use as the model configuration. By comparing the flow interaction with and without the plume also between laminar and turbulent models, Bakker concluded RANS (Reynolds-Averaged-Navier-Stokes) calculations with transport equations turbulence models reproduce the general organization of the flow but the afterbody wall-pressure profile on the boat-tail cannot be predicted accurately due to the fact that the turbulence models have difficulties to reproduce positive pressure gradients. Lee [105] investigated the PIFS at high plume to exit pressure ratio. The shock position and the extent of the flow separation were analyzed by varying the freestream Mach number as well as the plume to exit pressure ratio. Different models of afterbody configurations were also studied numerically. The results suggested that with the rounded afterbody configuration, the plume-induced shock can be moved downstream and to reduce the shock-induced separation bubble. Van Oudheusden [106] studied the base-flow/plume interaction by carrying out the PIV investigation experimentally. Underexpanded jet flow with freestream Mach number of 2 and 3 were used as the flow conditions. The 3D numerical LORE code was used to simulate the flow field. A quantitative comparison between the numerical and experimental resulted showed the base-flow/plume interaction phenomena can be accurately studied by means of PIV. Kim [107-108] et al., investigated the PIFS phenomenon on different afterbody configurations. The boat-tail, straight and flare were used as computational models. The results showed that the boat-tailed afterbody configuration tended to cause the PIFS while the flare configuration suppressed PIFS. Kim also compared the PIFS with different chamber to freestream pressure ratios on the straight type afterbody configuration. The pressure contours showed that with the increase of the chamber to freestream pressure ratio, the size of the recirculation region decreased and the position of the region moves toward a point on the edge of the model where the pressure ratio is 1/3, and the

PIFS originated at that edge. The size of the PIFS increased with a further increase of the chamber to freestream pressure ratio. Gusman [109] et al., studied the numerical simulation of PIFS on Saturn V launch vehicle. The OVERFLOW CFD code was used to simulate the Saturn V launch vehicle including plumes at four points in the ascent trajectory. The PIFS distance had been determined and the non-dimensional wall spacing $y^+ = 0.9$ was proved that can provide sufficient resolution for predicting PIFS distance. Deere [110] et al., carried the similar study of PIFS on Saturn V launch vehicle. The USM3D CFD code was evaluated to calculate the PIFS for the use with liquid-fuel rockets—Saturn V. A recommended process of calculating PIFS with USM3D was established.

1.5 Thermal Radiation Effects on Plume Induced Flow Interaction

When considering a missile or launch vehicle uses solid propellants, the exhaust plume contains complex mixture of gas at high temperature. In the case of solid propellants particles are included in the plume as the products of combustion, the distribution of temperature of the plume will be affected due to fact that the particles will influence the radiative heat flux, and which varies with particle size, absorption coefficient and the altitude, etc. It is one of the main issues that will affect the PIFS or base-flow/plume interaction which eventually will cause rapid change of temperature along the launch vehicle surface body or the base [111-113]. This multi-species effect for plume that involves thermal radiative heat transfer has been investigated computationally and experimentally, considering different factors like the altitude [114], particle size, absorption coefficient [115], and different radiation computational models [116-117]. Rao [118-119] et al., and Alexeenko [120] et al., used different computational approaches to simulate the radiation effects of Atlas rocket plumes. Comparisons were made among several computational models, and the results showed that radiation calculation based on the soot-laden

flowfield showed better agreement to the experimental data, which demonstrated that the soot could be the major radiator for the solid propellant rocket with multi-phase flow.

1.6 Objectives and Dissertation Organization

The objective of this study is to analyze the micro- and small-scale converging-diverging nozzle and the corresponding plume induced flow separation computationally. Different numerical cases are investigated to complete the parametric studies in order to obtain a better understanding of plume induced flow separation under different conditions.

The dissertation is organized into 5 chapters. Chapter 2 presents the “Saw Tooth” surface modification applied on microscale converging-diverging nozzle in order to reduce viscous effects and improve the system performance. Chapter 3 illustrates the plume induced flow separation (PIFS) on miniaturized CD nozzle by carrying out the steady-state computational solution. Chapter 4 focuses on the transient analysis of plume induced shockwave motion and the plume induced flow separation (PIFS) phenomenon on miniaturized CD nozzle. Chapter 5 provides the conclusions and discussions.

CHAPTER 2

CD MICRONOZZLES: PERFORMANCE ENHANCEMENT VIA SURFACE MODIFICATION

Submitted to *Journal of Propulsion and Power*, April 2014

This chapter provides a detail description of viscous effects on microscale converging-diverging nozzle and the application of “Saw Tooth” surface modification in order to reduce the viscous forces and improve the nozzle performance.

2.1 Significance of Viscous Effects on Microscale Converging-Diverging Nozzle

In order to illustrate the viscous effects on microscale Converging-Diverging nozzle, the following section provides different parametric computational studies to show the decreasing of nozzle performance when the viscous effects increase.

2.1.1 Mathematical Formulation

A schematic diagram of the conical microscale CD nozzle with a smooth throat transition and without surface modification is shown in Fig. 1. The design strategy of the nozzle throat transition follows that outlined in Liu et al. [86]. The half-angle of the divergent region of the nozzle for all cases was held constant ($\theta = 15^\circ$) as was the expansion ratio ($\varepsilon = 17$), which is the same configuration used by Bayt [31].

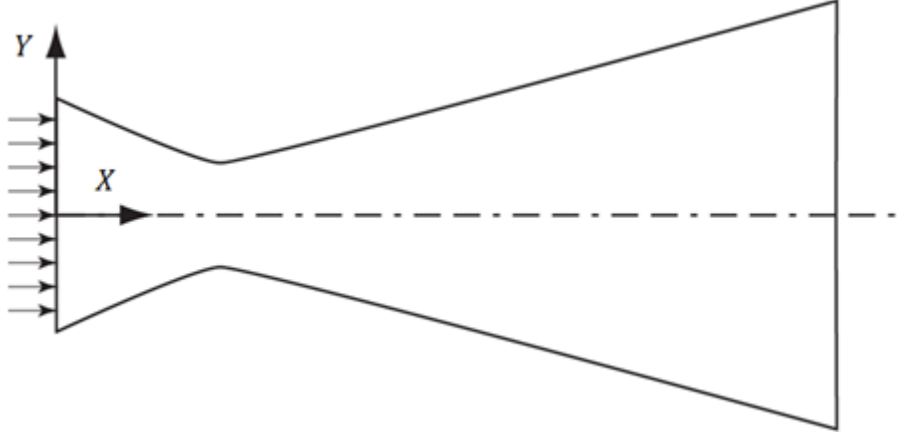


Fig.1 A schematic diagram of the microscale CD nozzle without surface modification

An axisymmetric computational model was used to examine the flow field and performance metrics. The axisymmetric form of compressible continuity, Navier-Stokes, and energy equations used in this study are given as

$$\frac{\partial}{\partial t} \rho + \nabla \cdot (\rho \mathbf{V}) = 0 \quad (6)$$

$$\frac{\partial}{\partial t} (\rho \mathbf{V}) + \nabla \cdot (\rho \mathbf{V} \mathbf{V}) = -\nabla p + \nabla \cdot (\boldsymbol{\tau}) \quad (7)$$

$$\frac{\partial}{\partial t} (\rho E) + \nabla \cdot (\mathbf{V}(\rho E + p)) = \nabla \cdot (k \nabla T + (\boldsymbol{\tau} \cdot \mathbf{V})) \quad (8)$$

The relation between energy and enthalpy is given as

$$E = h - \frac{p}{\rho} + \frac{\mathbf{V}^2}{2} \quad (9)$$

and by definition

$$h = \int_0^T c_p dT \quad (10)$$

The constitutive relation for stress in a Newtonian fluid is given as

$$\boldsymbol{\tau} = \mu \left[(\nabla \mathbf{V} + \nabla \mathbf{V}^T) - \frac{2}{3} (\nabla \cdot \mathbf{V}) \mathbf{I} \right] \quad (11)$$

The equation of state for the fluid within the nozzle is assumed to be that of an ideal gas

$$p = \rho RT \quad (12)$$

The thermo physical properties of specific heat and dynamic viscosity were respectively modeled using a fifth order polynomial [123] and the power law [124].

A detailed description of the boundary conditions used to solve the above mathematical formulation is provided in the following section.

2.1.2 Numerical Method

The governing equations were solved using the commercially available CFD package ANSYS-FLUENT version 13.0. A structured grid was generated using ANSYS Workbench. A typical computational grid is shown in Fig. 2. The computational domain outside the nozzle has been truncated in the figure. The entire computational domain is not shown in the figure so that a more detailed representation of the computational grid within the CD nozzle may be presented.

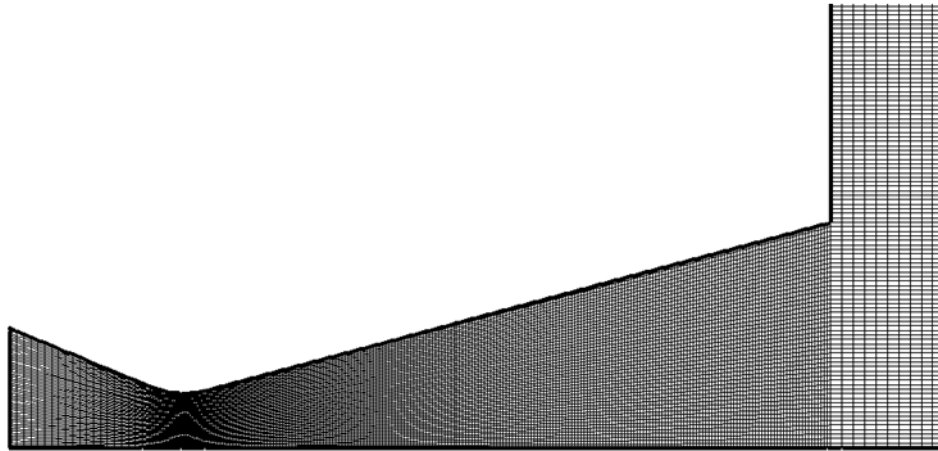


Fig.2 A domain highlighting the structure of typical grid in the micronozzle

The boundary conditions applied to the computational domain were:

- Nozzle Inlet – pressure inlet/isothermal,
- Nozzle Wall – no-slip/adiabatic wall, and
- External to the nozzle – pressure outlet/isothermal.

Justification of the no-slip boundary conditions along the internal surface of the CD nozzle will be outlined later. Specification of the inlet pressure requires a user input of total and static pressure. From this input, isentropic relations are used to evaluate the velocity magnitude at the boundary. Individual velocity components are determined using the direction vector components of the boundary. Specification of the outlet pressure requires a user input of the static pressure at the associated boundary. The no-slip boundary conditions assume that the normal and tangential velocity components at the nozzle wall are identically zero. Isothermal boundary conditions require the user to define a constant temperature at the associated boundary. Adiabatic wall conditions require that the temperature gradient normal to the surface is identically equal to zero.

Density-velocity coupling, for the above mentioned governing equations and boundary conditions, was achieved using a coupled implicit solver [127]. A second-order upwind scheme [128] was used to discretize advective terms. The steady-state computational results are spatially second-order accurate.

2.1.3 Verification & Validation

A study was conducted to determine under what conditions the results would be grid independent. The spatial profile of the Mach number at the nozzle exit plane was used to determine grid independence. Initially, the Mach number profile was calculated using results from a computational domain with 4,000 cell. The number of cells in the computational domain was progressively increased until the calculated Mach number profile of two consecutive grid resolutions were within a maximum of 1% of each other. Using this criterion, it was determined that a computational domain with 32,000 cells was sufficient to produce grid independent results.

The computational results were validated by comparison with the computational and experimental results of Bayt [129]. As can be seen from Fig. 3, the trend in the computational results from this study agreed well with those of Bayt. The maximum deviation from Bayt's computational data was 0.52%.

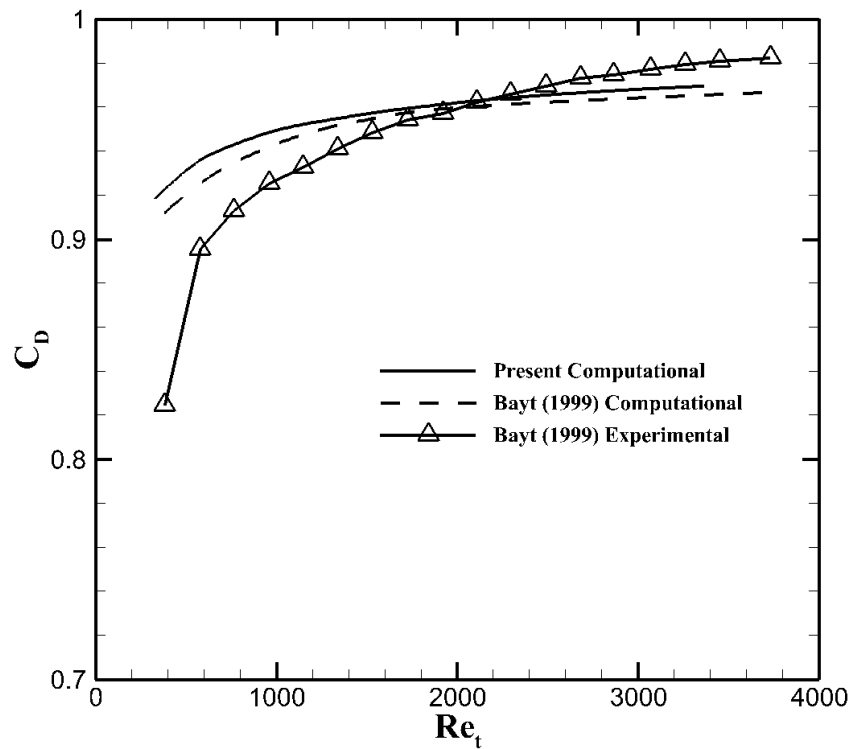


Fig.3 Validation of computational model

As such, the results of this study may be considered valid. Table 1 provides a listing of the parameters used to generate the computational results and Table 2 provides a mapping of the throat radius with the respective case number.

Table 1: Baseline parameters used to generate computational results

P_o (Pa)	1.3×10^6
T_o (K)	300.0
γ	1.4
P_b (Pa)	4.0×10^3
θ ($^\circ$)	15
ε	17

Table 2: Values of throat radius considered

Case Number	R_t (μm)
1	80
2	60
3	50
4	40
5	30

2.1.4 No-Slip Boundary Condition: Justification

Prior to conducting a parametric study to determine the impact on nozzle performance, the no-slip boundary assumption was tested by examining the magnitude of the Knudsen number.

The Knudsen (Kn) number can be defined locally as [34]

$$\text{Kn} = \frac{\lambda}{l} \quad (13)$$

where the flow field characteristic length is defined as

$$l = \frac{\rho}{|\nabla \rho|} \quad (14)$$

The various flow regimes associated with the magnitude of the Knudsen have historically been categorized as [60]

- continuum flow ($\text{Kn} < 0.01$)
- slip flow ($0.01 < \text{Kn} < 0.1$)
- transitional flow ($0.1 < \text{Kn} < 10$)
- free molecular flow ($\text{Kn} > 10$)

To determine the associated flow regime, the nozzle with the smallest throat diameter considered in this study was examined. Fig. 4 presents a contour plot of the Knudsen number for the flow conditions outlined in Table 1. As can be seen from the figure, the largest Kn is $\mathcal{O}(10^{-3})$ and therefore the entire internal flow field is in the continuum flow regime. As such, the continuum CFD solver and the no slip boundary conditions are applicable for this study.

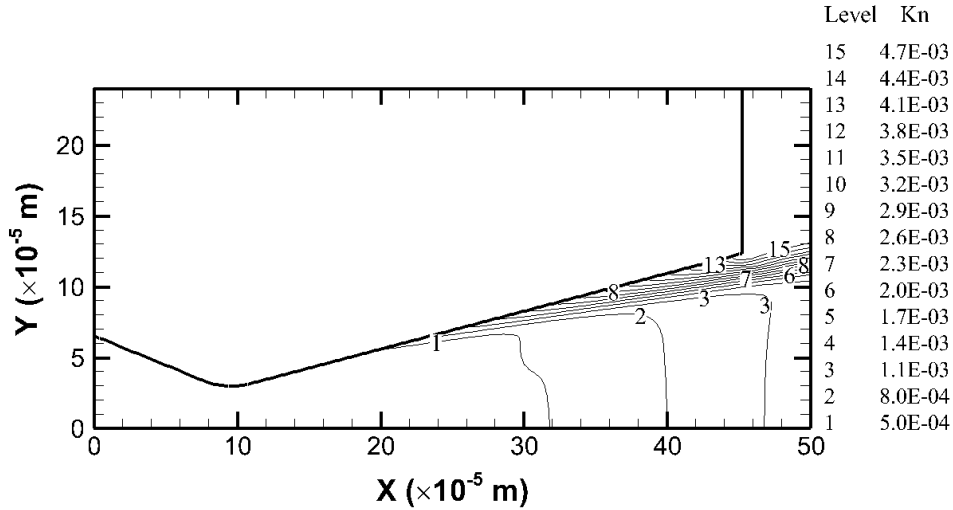
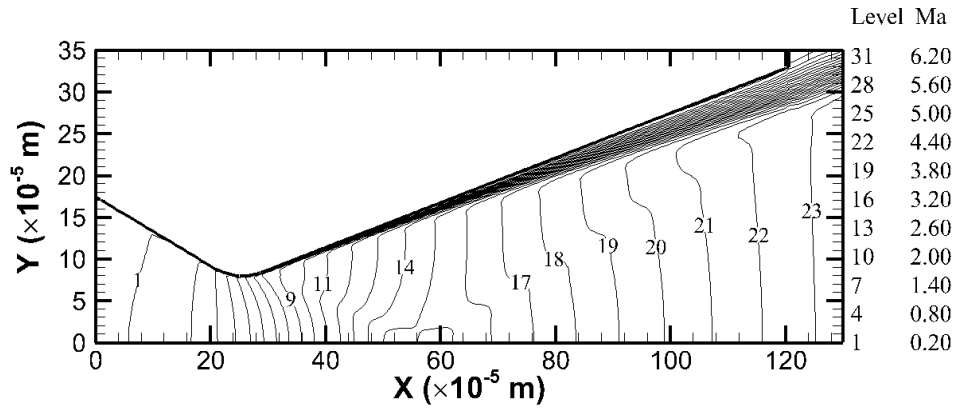


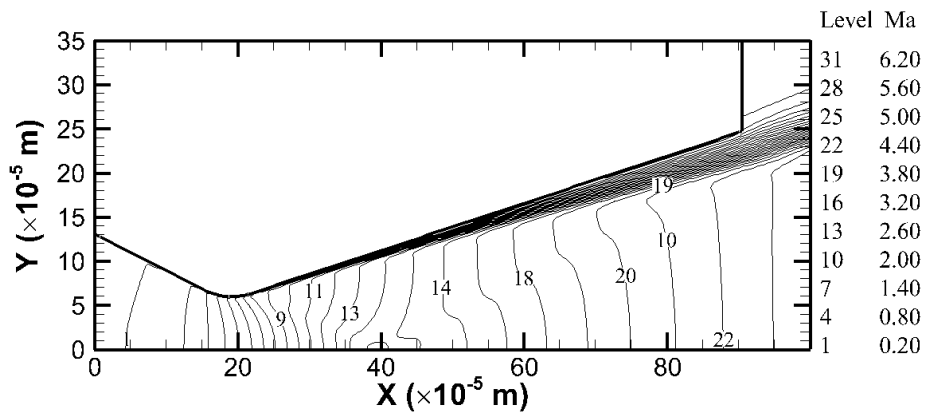
Fig.4 Kn contour for case 5 ($R_t = 30 \mu\text{m}$)

2.1.5 Internal Converging-Diverging Nozzle Flow: Viscous Effects

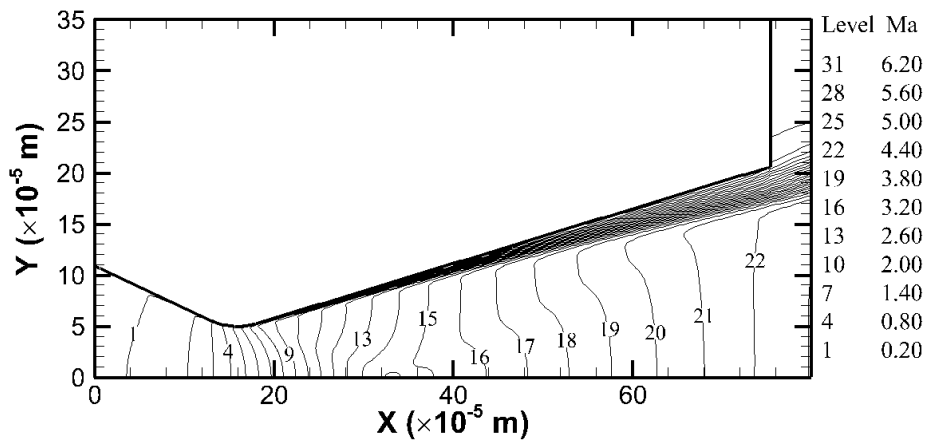
As one might expect, the importance of viscous forces becomes more significant as the geometric size of the nozzle decreases. This is because the wall shear stress is inversely proportional to the geometric characteristic length, i.e. $\tau \propto 1/y$. As the geometric characteristic length decreases, the size of the inviscid core must also decrease thereby producing a negative impact on nozzle performance relative to the inviscid case. Fig. 5 provides a comparison of the Mach number contours for the five cases considered in this study.



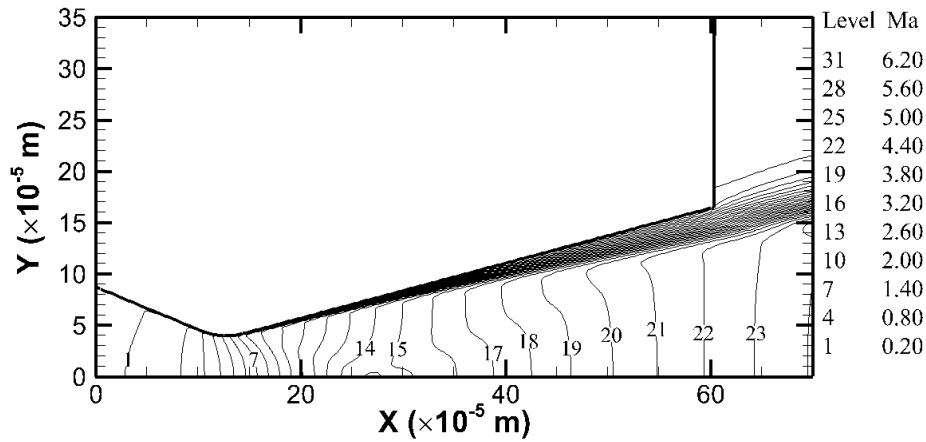
(a) Case 1 ($R_t = 80 \mu\text{m}$)



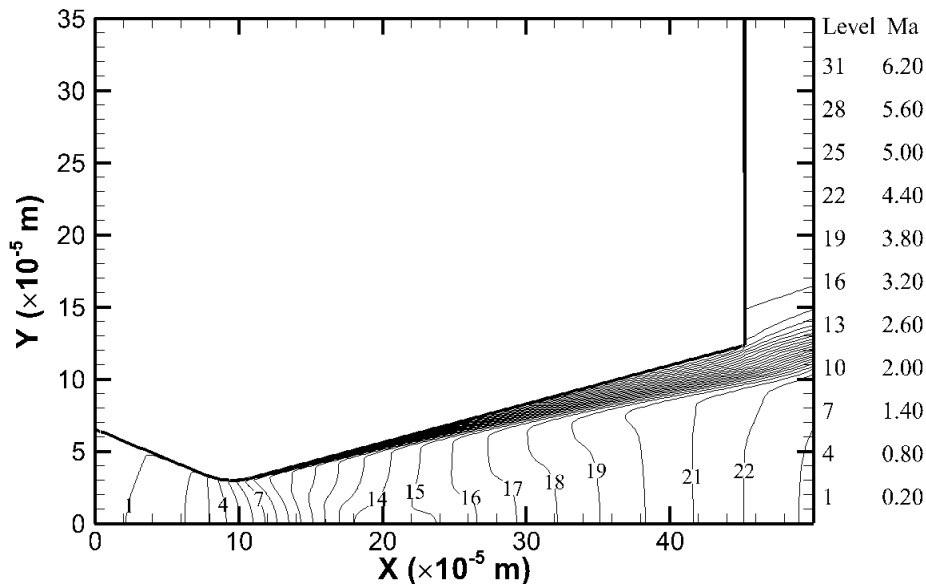
(b) Case 2 ($R_t = 60 \mu\text{m}$)



(c) Case 3 ($R_t = 50 \mu\text{m}$)



(d) Case 4 ($R_t = 40 \mu\text{m}$)



(e) Case 5 ($R_t = 30 \mu\text{m}$)

Fig.5 Mach contour for case 1 ($R_t = 80 \mu\text{m}$) to case 5 ($R_t = 30 \mu\text{m}$)

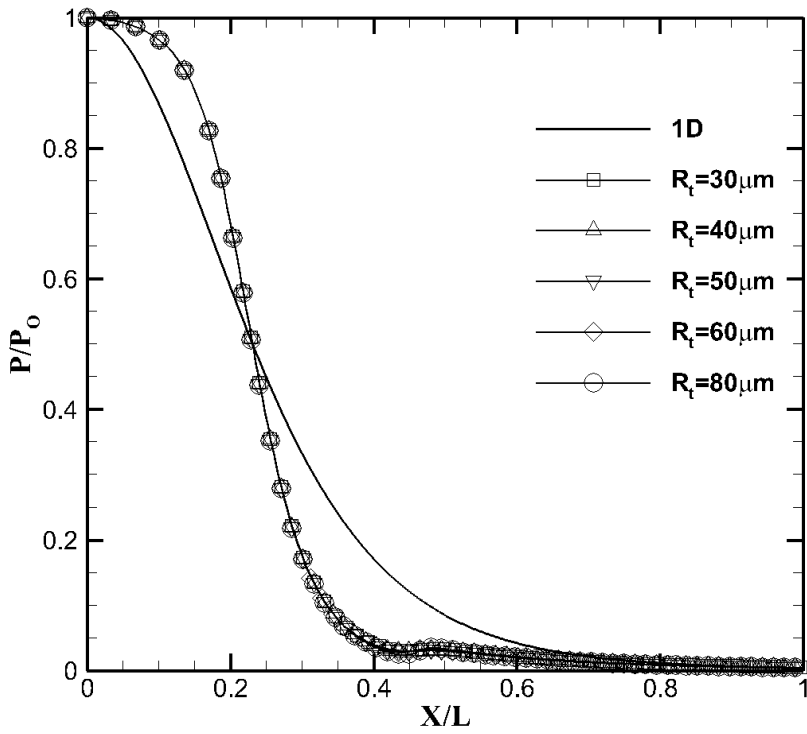
It is important to note that the numbers appearing on the plot represent contour line numbers and not Mach number. The Mach number corresponding to the contour line number is shown in the plot legend. As expected, the viscous region at the nozzle exit increases with decreasing nozzle size. In this study, the viscous region was taken to be the distance from the

surface to a point in the vertical direction where the flow speed increased to 99% of that at the nozzle centerline, i.e.

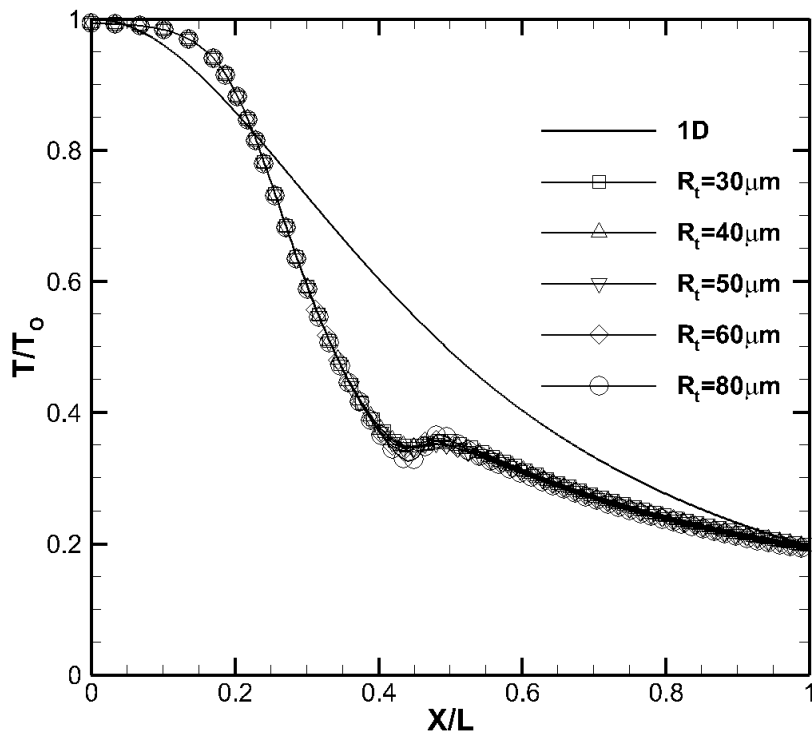
$$\delta_{\text{exit}}|_{v/v_{cl}} < 0.99 \quad (15)$$

As can be seen from Fig. 5, the mean exit Mach number decrease by 2.38%, from 4.62 to 4.51, for a corresponding decrease in the throat diameter of 80 μm to 30 μm . This decrease is due to the relative increase in the viscous region associated with the decrease in nozzle size.

Fig. 6 presents a comparison between results from a one-dimensional isentropic flow model and the fully viscous axisymmetric flow model considered in this study. The ratio of pressure and temperature as well as the 1-D isentropic relations along the nozzle centerline are plotted in Fig. 6. From the case $R_t = 80\mu\text{m}$ to case $R_t = 30\mu\text{m}$, the averaged centerline temperature increased by about 1.03%. The visible “bump” in Fig.7 is provoked by a weak internal shock, which originates at $x/L=0.45$, near the throat edge and reflects on the centerline [29]. The points where the isentropic predictions cross that of the fully viscous models for pressure ratio and temperature ratio, as shown in Fig.7, occurs at the nozzle throat.



(a) Pressure ratio along the nozzle centerline



(b) Temperature ratio along the nozzle centerline

Fig.6 Pressure and temperature ratio along the nozzle centerline

Two parameters, the thrust coefficient (C_f) and specific impulse efficiency ($I_{sp}/I_{sp,inviscid}$) are used to evaluate the micronozzle performance, which are defined in equations (16)—(18) [7] [130]. The $I_{sp,inviscid}$ refers to the specific impulse of the inviscid flow condition.

$$C_f = \frac{F_t}{A_t P_o} \quad (16)$$

$$I_{sp} = \frac{F_t}{\dot{m} g_o} \quad (17)$$

$$F_t = \int_{A_{exit}} (\rho u_e^2 + P_e) dA_{exit} \quad (18)$$

Fig. 7 and Fig. 8 show the corresponding performances with the throat radius (R_t). The results showed that the thrust coefficient decreased by about 2.13% and the specific impulse efficiency dropped by about 1.11% from cases 1 to 5, which is due to the decreasing of the nozzle size, the viscous effects increased and resulted in the decreasing of the nozzle performances.

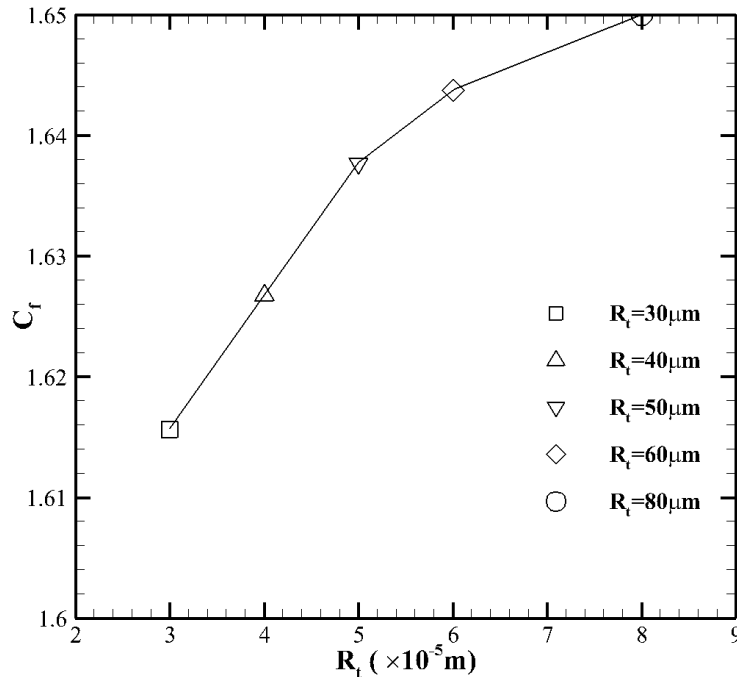


Fig.7 Discharge coefficient (C_f) for $R_t = 30 \mu\text{m}$ to $R_t = 80 \mu\text{m}$

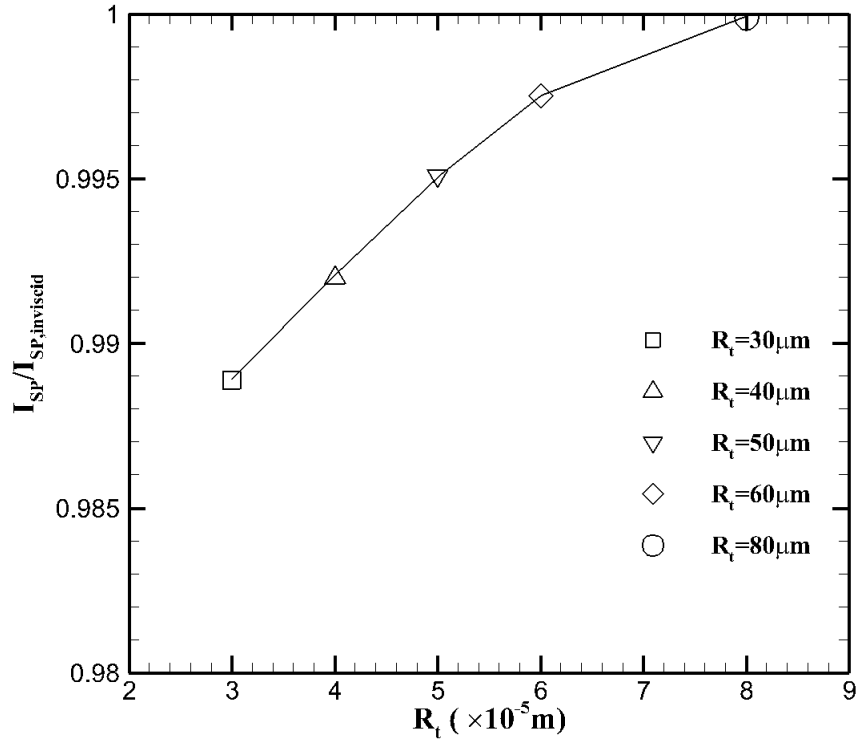


Fig.8 Specific impulse efficiency ($I_{sp}/I_{sp,inviscid}$) for $R_t = 30 \mu\text{m}$ to $R_t = 80 \mu\text{m}$

Another parameter, the viscous region ratio, which is defined by the area ratio A_{visous}/A_{exit} , where A_{visous} associated with the viscous region at the nozzle exit plane. Fig. 9 shows the viscous region ratio at the nozzle exit from cases 1 to 5. It was calculated that the viscous region obstructed up to about 5% of the nozzle exit area when the nozzle size decreased from $R_t = 80\mu\text{m}$ to case $R_t = 30\mu\text{m}$.

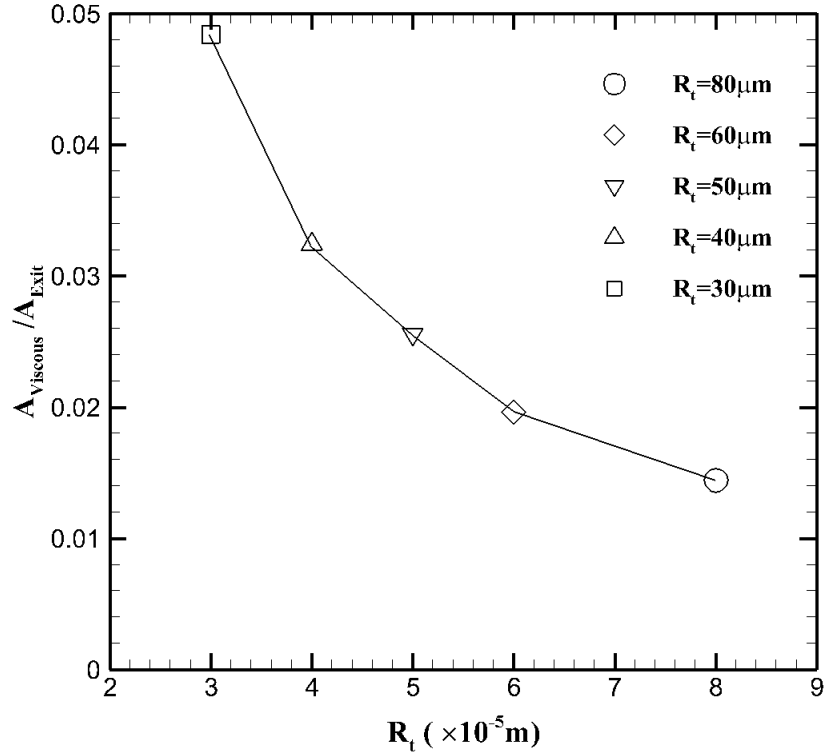


Fig.9 Viscous region ratios for $R_t = 30 \mu\text{m}$ to $R_t = 80 \mu\text{m}$

The above results clearly illustrated that the significance of viscous effects due to geometric scaling. With decreasing nozzle size, the corresponding nozzle performances metrics, thrust coefficient (C_f) and specific impulse efficiency ($I_{sp}/I_{sp,invicid}$), decreased while the viscous region increased at the exit plane.

2.2 “Saw Tooth” Surface Modification

Due to the fact that micro-scale nozzle performance is strongly influenced by the viscous forces, a saw-tooth wall modification was introduced with the goal of reducing such forces. As case 5 ($R_t = 30 \mu\text{m}$) represented the smallest throat radius, it was used to test this hypothesis. Fig. 10 provides an example of the surface modification pattern. As can be seen from the figure 10, right triangles perpendicular to the nozzle wall were used to simulate the saw-tooth pattern.

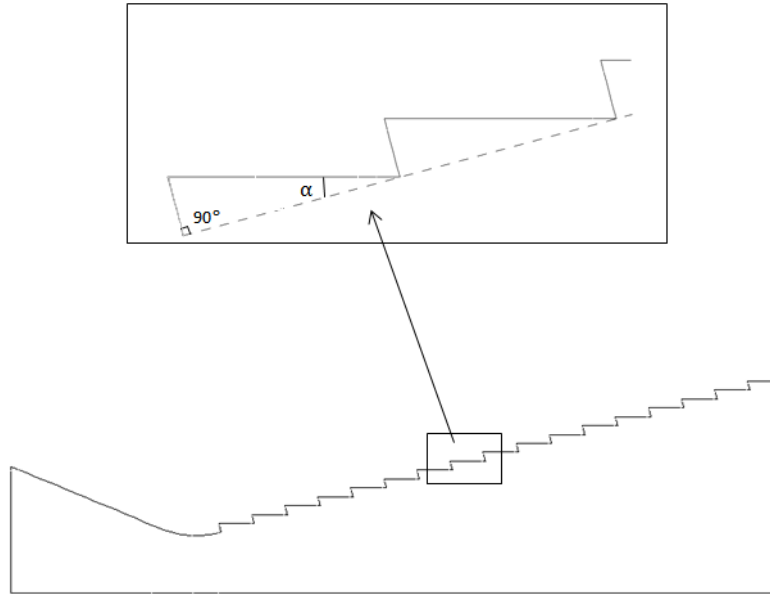


Fig. 10 “Saw Tooth” nozzle wall configuration

2.2.1 Justification of No-Slip Boundary Condition for “Saw Tooth” Modification

The first set of computational experiments varied the number of saw teeth with a constant saw tooth angle of 15° . Four different conditions were examined: $N = 10$, $N = 20$, $N = 40$ and $N = 60$. Fig. 11 shows the Kn contour for $N = 60$.

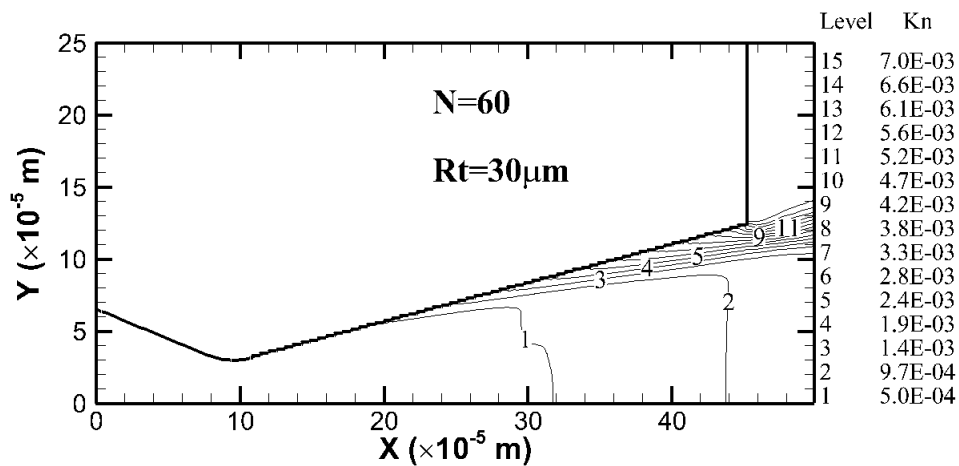
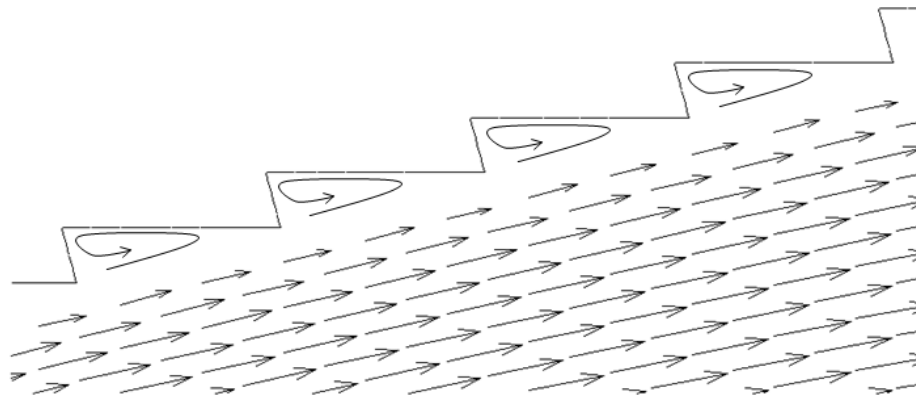


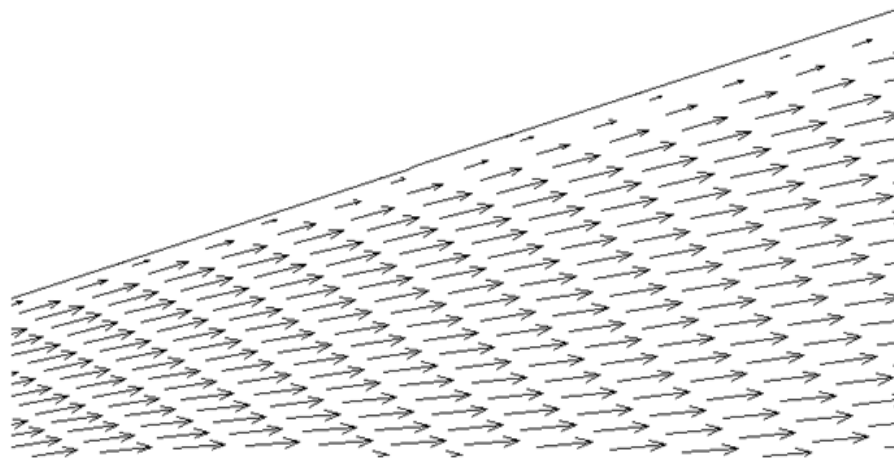
Fig.11 Kn contour for N = 60

2.2.2 “Saw Tooth” Surface Modification Flow Illustration

Fig.12 (a) provides a schematic diagram of the expected flow conditions in the vicinity of the saw tooth surface modification while Fig.12 (b) shows the expected flow pattern for the nozzle without the surface modification. It was anticipated that the flow within the cavities formed by the saw teeth would result in an effective slip flow near an effective boundary formed by an imaginary line corresponding to the nozzle wall without a saw tooth surface modification. If such a slip boundary were occurring, then the result would be to decrease the viscous forces in the vicinity of the wall.



(a) Flow conditions of “Saw Tooth” nozzle wall



(b) Flow conditions of smooth nozzle wall

Fig. 12 Flow conditions illustrations for two types of nozzle wall

Fig. 13 shows the computational result of flow pattern for the case that the saw teeth number $N=40$. As can be observed in Fig.13, vortices are generated inside the cavities formed by the saw teeth.

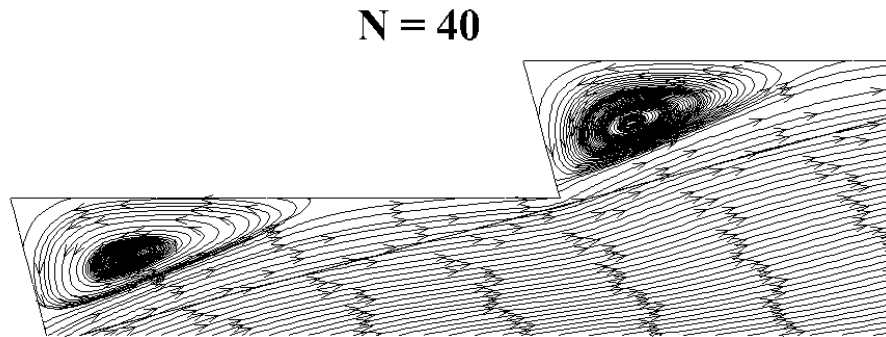


Fig. 13 Streamline near the wall for $N=40$

2.2.3 Performance of “Saw Tooth” Surface Modification on Micronozzle

Mach number contours for nozzle with saw-tooth surface modification with number of teeth $N=60$ is shown in Fig.14. It was calculated that the exit mean Mach number was 4.78 for the case with $N=60$ and the nozzle has a throat radius of $R_t = 30 \mu\text{m}$. Exit mean Mach number was calculated to be 4.71 for the nozzle without the saw-tooth surface modification with a throat radius of $R_t = 30 \mu\text{m}$. The exit mean Mach number increased by about 1.5%. The increasing of the exit mean Mach number indicates that when applied the saw-tooth wall surface modification with the saw teeth number $N=60$, the viscous forces were decreased and resulted an increasing of exit Mach number.

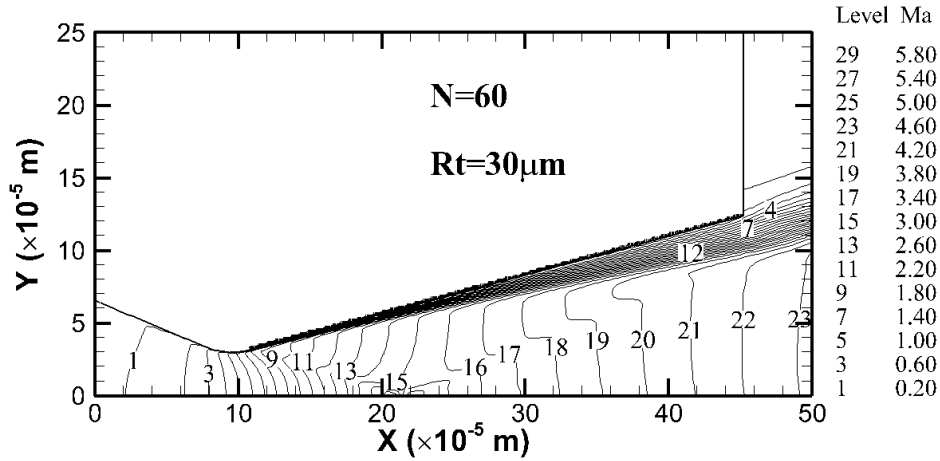


Fig.14 Mach contour for N=60

Two parameters, the thrust coefficient (C_f) and specific impulse efficiency ($I_{sp}/I_{sp,inviscid}$), as defined from equation (14) to (16), were calculated and are shown in Fig. 15 and Fig. 16. The number of saw teeth used to compare the results are $N=0$, $N=10$, $N=20$, $N=40$ and $N=60$, with the nozzle has a throat radius of $R_t = 30 \mu\text{m}$. For the case when $N=0$, which is the nozzle without the saw tooth surface modification, the thrust coefficient (C_f) was calculated as in $C_f = 1.437$, and the specific impulse efficiency ($I_{sp}/I_{sp,inviscid}$) was about 0.916. For the case when $N= 60$, which is the nozzle applied the saw-tooth surface modification with the number of saw teeth $N=60$, it was calculated that the thrust coefficient $C_f = 1.449$ and the specific impulse efficiency ($I_{sp}/I_{sp,inviscid}$) is 0.924. The thrust coefficient (C_f) and the specific impulse efficiency ($I_{sp}/I_{sp,inviscid}$) increased by about 0.83% compared to the case that the nozzle without the saw-tooth surface modification. The calculations and comparisons of the thrust coefficient (C_f) and specific impulse efficiency ($I_{sp}/I_{sp,inviscid}$) indicated that for the nozzle with a throat radius of $R_t = 30 \mu\text{m}$, saw teeth angle of $\alpha = 15^\circ$, the application of saw-tooth surface modification with an increasing of saw teeth number from $N=0$ to $N=60$ resulted an increasing of nozzle performance, i.e. the thrust coefficient and the specific impulse efficiency.

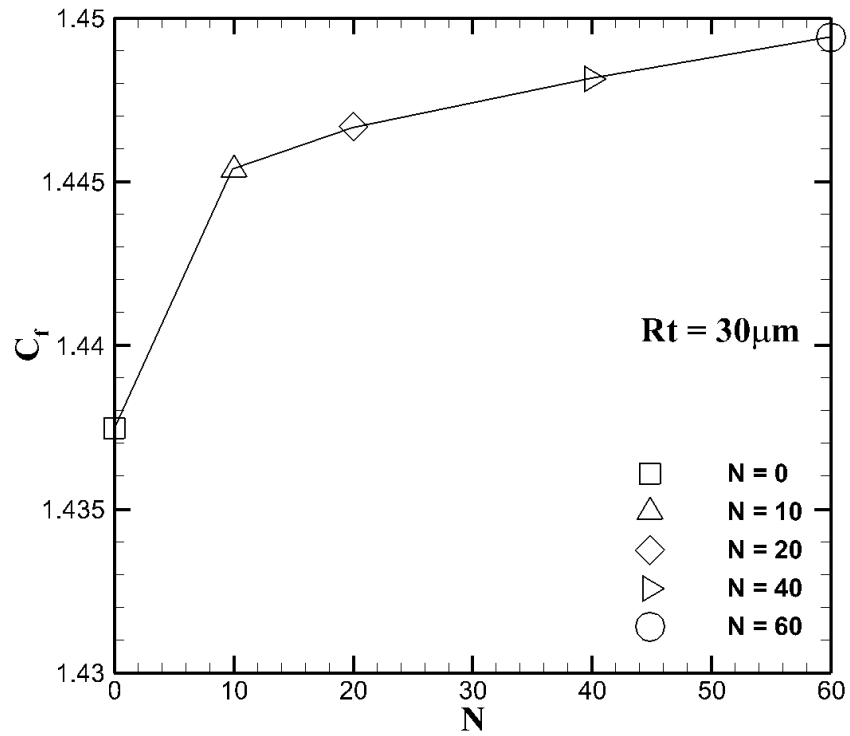


Fig.15 Thrust coefficient (C_f) for $N = 0$ to $N = 60$

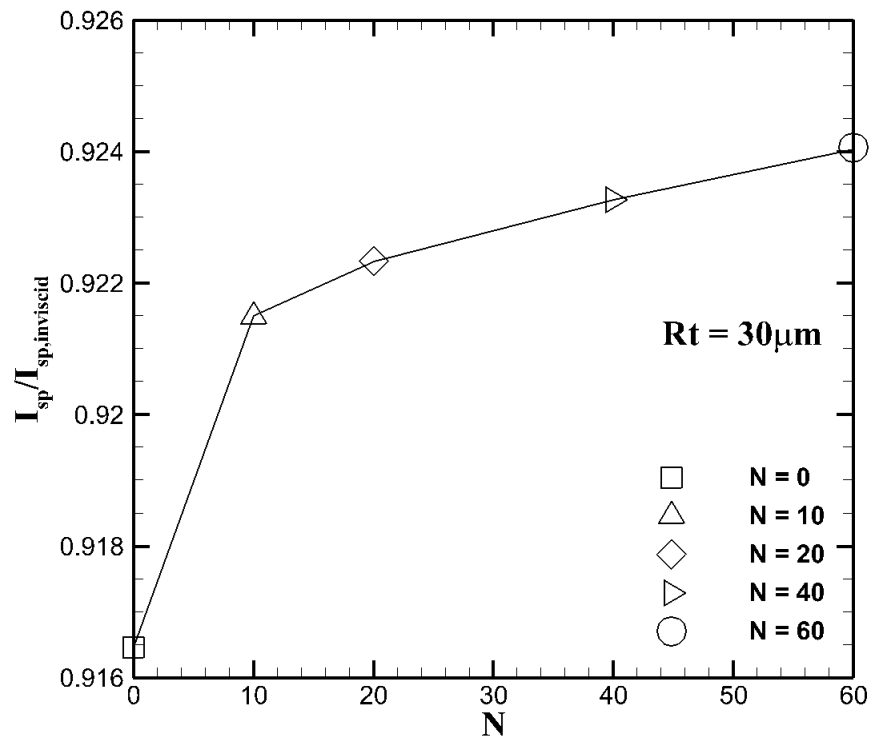


Fig.16 Specific impulse efficiency ($I_{sp}/I_{sp,inviscid}$) for $N = 0$ to $N = 60$

Another factor considered in this study was the effect of saw teeth angle (α). Two additional numerical cases with saw teeth angles $\alpha = 25^\circ$ and $\alpha = 30^\circ$ were considered as the parametric studies. The thrust coefficient (C_f) and specific impulse efficiency ($I_{sp}/I_{sp,invicid}$) were also calculated and compared to illustrate the effect of the saw teeth angle (α). The results are shown in Fig. 17 and Fig. 18. For the case with saw teeth number $N=60$ and saw teeth angle $\alpha = 30^\circ$, it was calculated that the thrust coefficient $C_f = 1.45$, and the specific impulse efficiency ($I_{sp}/I_{sp,invicid}$) is 0.924. The previous results showed that for the case without the saw tooth surface modification ($N=0$), the thrust coefficient $C_f = 1.437$ and the specific impulse efficiency ($I_{sp}/I_{sp,invicid}$) is 0.916. By increasing the saw teeth angle to $\alpha = 30^\circ$ for the case with the number of teeth $N=60$, the thrust coefficient (C_f) and the specific impulse efficiency ($I_{sp}/I_{sp,invicid}$) increased by about 0.9% compared to the case that the nozzle without saw-tooth surface modification.

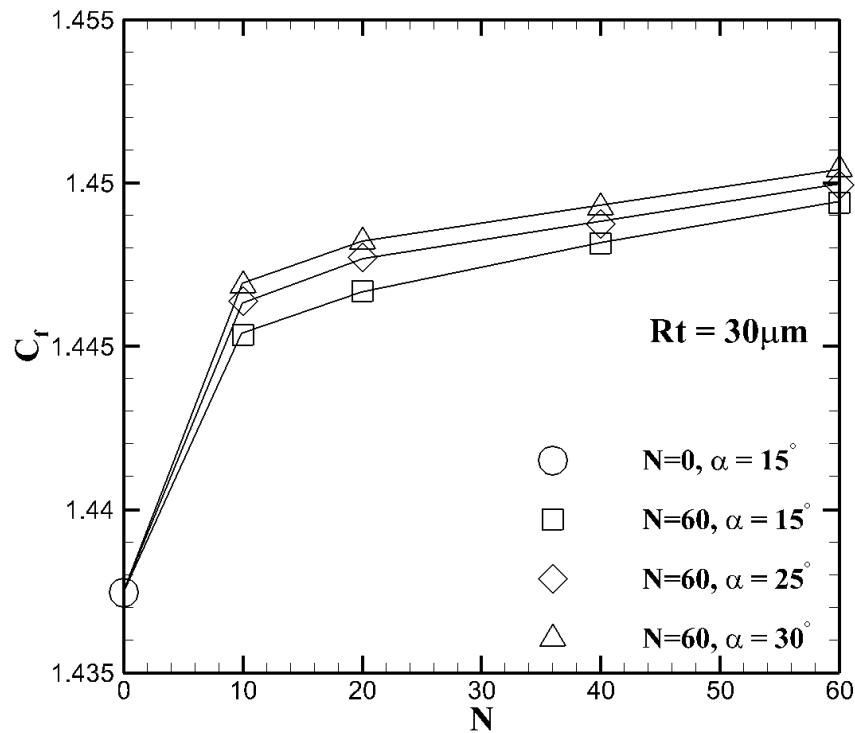


Fig.17 Thrust coefficient (C_f) for $N = 60$ from $\alpha = 15^\circ$ to $\alpha = 30^\circ$

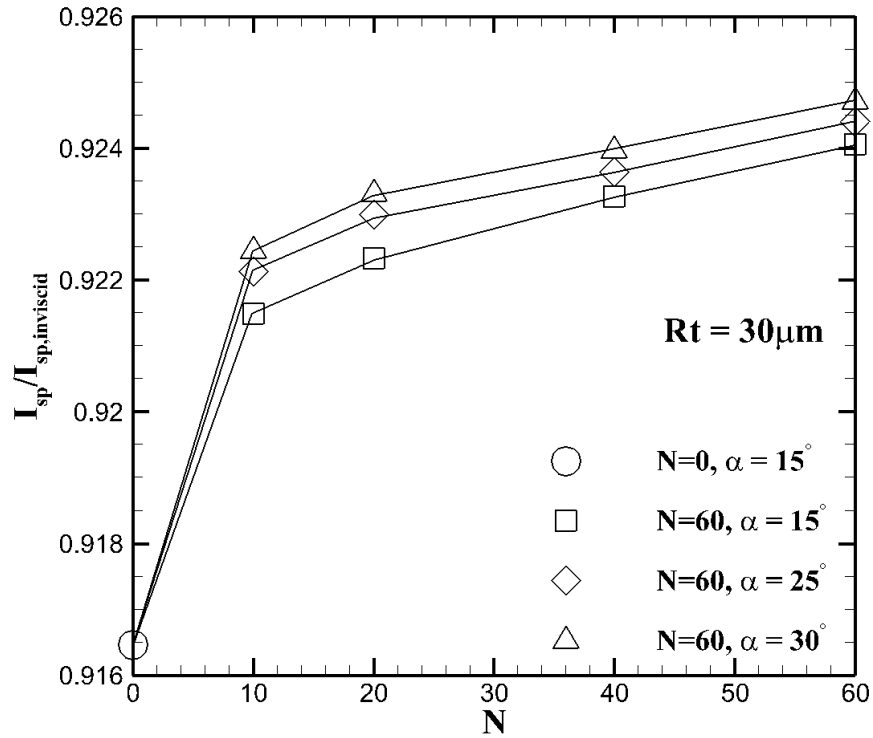


Fig.18 Specific impulse efficiency for $N = 60$ from $\alpha = 15^\circ$ to $\alpha = 30^\circ$

The calculations and comparisons of the thrust coefficient (C_f) and specific impulse efficiency ($I_{sp}/I_{sp,invicid}$) by considering the saw teeth angle (α) indicated that the application of saw-tooth surface modification with an increasing of saw teeth angle resulted an increasing of the nozzle performance. By increasing the saw tooth angle, larger cavity areas were formed. This increase in cavity area resulted in more pronounced vortex generation within the cavities. The result was that the effective slip boundary was thus pronounced resulting in an increase in nozzle performance.

CHAPTER 3

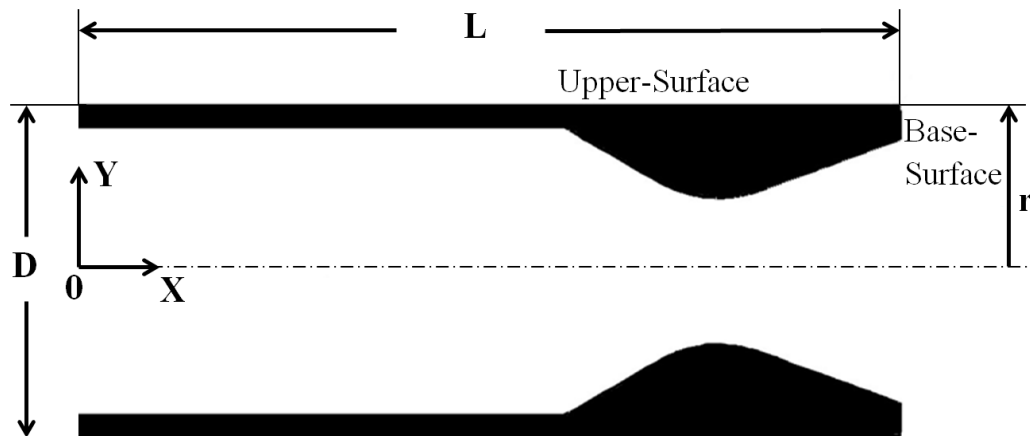
COMPUTATIONAL INVESTIGATION OF SCALING EFFECTS ON PLUME INDUCED FLOW SEPARATION (PIFS)

Submitted to *Journal of Computational Thermal Science*, April 2014

This chapter provides a detail description of plume induced flow separation (PIFS) phenomenon on CD nozzles (10^{-2} m to 10^{-3} m) that can be utilized on small-scale flight vehicle. The corresponding parametric studies are carried out to obtain a deep understanding of PIFS.

3.1 Computational Schematic and Mathematical Formulation

A schematic diagram of the conical microscale CD nozzle with a smooth throat transition is shown in Fig.19, as well as the plume induced flow separation (PIFS) phenomenon happens on a nozzle with straight afterbody configuration. The design strategy of the nozzle throat transition follows that outlined in Liu et al. [86], which is the same as discussed in Chapter 1. The half-angle of the divergent region of the nozzle for all cases was held constant ($\theta = 15^\circ$) and the designed nozzle exit Mach number is 3.0.



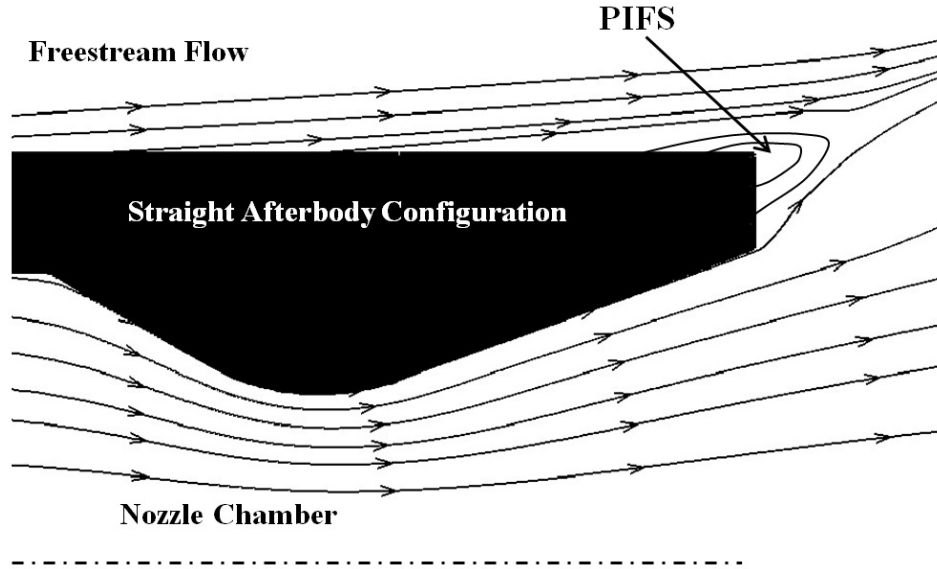


Fig.19 PIFS phenomena on a straight afterbody configuration

An axisymmetric computational model was used to examine the flow field and performance metrics. The compressible Reynolds-averaged Navier Stokes equations used in this study are given as:

$$\frac{\partial \bar{p}}{\partial t} + \frac{\partial}{\partial x_j} (\bar{p} \hat{u}_j) = 0 \quad (19)$$

$$\frac{\partial (\bar{p} \hat{u}_i)}{\partial t} + \frac{\partial}{\partial x_j} (\hat{u}_i \bar{p} \hat{u}_j) = -\frac{\partial p}{\partial x_i} + \frac{\partial \bar{\sigma}_{ij}}{\partial x_j} + \frac{\partial \tau_{ij}}{\partial x_j} \quad (20)$$

$$\frac{\partial (\bar{p} \hat{E})}{\partial t} + \frac{\partial}{\partial x_j} (\hat{u}_j \bar{p} \hat{H}) = \frac{\partial}{\partial x_j} (\bar{\sigma}_{ij} \hat{u}_i + \overline{\sigma_{ij} u_i''}) - \frac{\partial}{\partial x_j} (\bar{q}_j + \overline{c_p \rho u_j'' T''} - \hat{u}_i \tau_{ij} + \frac{1}{2} \overline{\rho u_i'' u_i'' u_j''}) \quad (21)$$

where

$$\hat{H} = \hat{E} + \bar{p} / \bar{\rho} \quad (22)$$

$$\bar{q}_j = -k \frac{\partial T}{\partial x_j} \quad (23)$$

The equation of state for the fluid within the nozzle is assumed to be that of an ideal gas

$$p = \rho RT \quad (24)$$

The thermo physical properties of specific heat and dynamic viscosity were respectively modeled using a fifth order polynomial [123] and the power law [124], as described in Chapter 1. A 2-equation $k\omega$ - shear stress transport (SST) model [125-126] was used for turbulence calculations.

A detailed description of the boundary conditions used to solve the above mathematical formulation is provided in the following section.

3.1.1 Numerical Method

The governing equations were solved using the commercially available CFD package ANSYS-FLUENT version 13.0. A structured grid was generated using ANSYS Workbench. Fig.2 shows the computational domain. The computational domain outside the nozzle has been truncated in the figure, so that a more detailed representation of the computational grid within the CD nozzle may be presented.

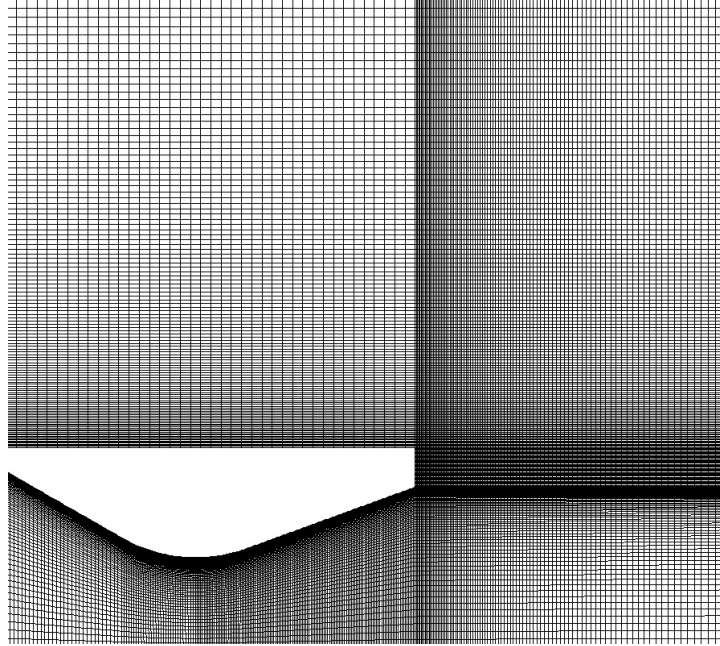


Fig.20 Computational domain

The boundary condition for nozzle inlet was used as in pressure inlet, which requires the input of total and static pressure and the isentropic relations are conducted to evaluate the velocity magnitude at the corresponding boundary. The nozzle wall was assumed to be no-slip, isothermal wall, which assumes the normal and tangential velocity components at the wall are zero and allows the constant temperature at the corresponding boundary. The boundary condition for the external domain to the nozzle was used as in pressure farfield, which requires the input of the static pressure and free stream Mach number and the density is calculated by using ideal-gas law under such boundary condition.

Density-velocity coupling was achieved using a coupled implicit solver [127]. A second-order upwind scheme [128] was used to discretize advective terms. The steady-state computational results are spatially second-order accurate.

3.1.2 Verification & Validation

A study was conducted to determine under what conditions the results would be grid independent. The static-to-ambient pressure ratio profile (P/P_∞) at the upper surface start from the nozzle exit was used to determine grid independence. Initially, the pressure ratio profile was calculated using results from a computational domain with 20,000 cells. The number of cells in the computational domain was progressively increased until the calculated pressure ratio profile of two consecutive grid resolutions were within a maximum of 1% of each other. Using this criterion, it was determined that a computational domain with 98,000 cells was sufficient to produce grid independent results.

The computational results were validated by comparison with the computational and experimental results of Lee [105]. As can be seen from Fig. 21, the trend in the computational results from this study agreed well with those of Lee. The maximum deviation from Lee's experimental data was 5.45%. As such, the results of this study may be considered valid.

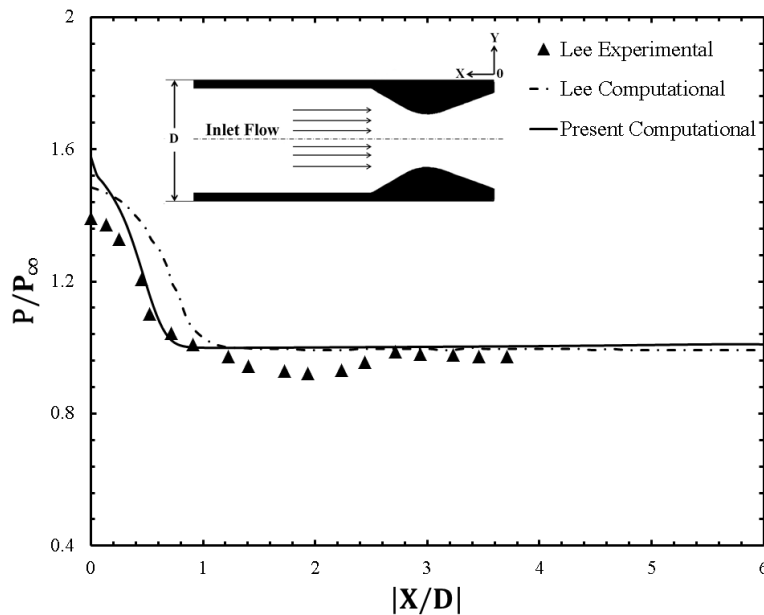


Fig.21 Validation of computational model

3.2 Results & Discussion

3.2.1 Effects of Pressure Ratio (PR) on Plume Induced Flow Separation (PIFS)

The effects of PR on base-flow/plume interaction and plume induced flow separation (PIFS) were analyzed numerically. The parameters considered are listed in Table 3. The pressure ratios PR=60, PR=120, PR=180 and PR=240 are used. Freestream Mach number under consideration is $Ma_\infty = 1.2$ and the freestream flow Reynolds number is $Re_\infty = 5.79 \times 10^6$.

Table 3 Baseline Parameters considered for the Pressure Ratio (PR) Effect.

PR	60	120	180	240
Ma_∞	1.2			
Re_∞	5.79×10^6			

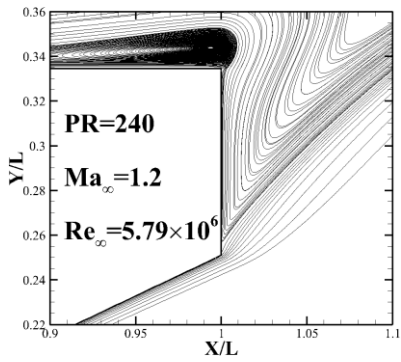
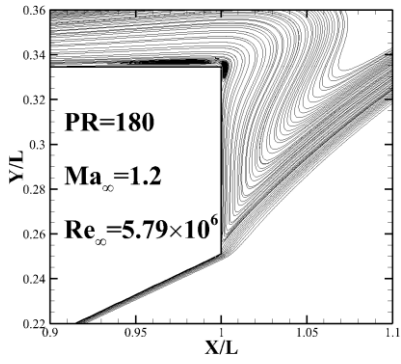
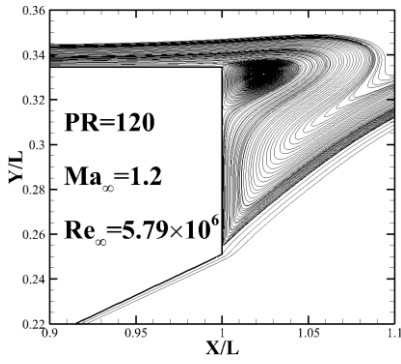
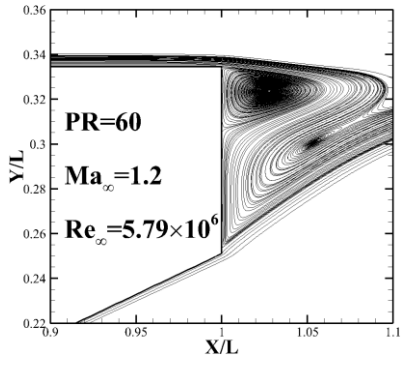


Fig.22 Pressure Ratio (PR) Effects on PIFS and Base-Flow/Plume Interaction

Fig.22 shows the streamline of pressure ratio effects. As can be seen in Fig.22, when pressure ratio $PR=60$, the flow-recirculation zone forms on the base-surface and results the base-flow/plume interaction. When the altitude increases and leads to an increase of chamber-to-ambient pressure ratio, from $PR=60$ to $PR=120$, the flow-recirculation zone decreases in size, and the location of this zone moves toward the upper-surface. With a further increase of pressure ratio, $PR=180$, the plume induced flow separation (PIFS) originates at $X/L = 1$. Any further increase of the pressure ratio results the formation of plume induced flow separation (PIFS) on the upper-surface, as can be seen in Fig. 22 with $PR=240$. With the increase of the altitude, the ambient pressure decreases due to the density decrease of the air (Giancoli, D., 2004), the pressure ratio between the nozzle chamber and ambient increases, which causes the exhaust plume to expand more in size. Thus, the interaction between the plume and the freestream flow happens, and generates the flow-recirculation zone due to the existence of the adverse pressure gradient. When the pressure ratio continues increasing, the exhaust plume experiences a further expansion in size and continues interact with the freestream flow, eventually the flow-recirculation zone is generated on the upper-surface and causes the flow-separation, which is the plume induced flow separation (PIFS). Further increase of pressure ratio allows the increase of the adverse pressure gradient in PIFS and results in the size increasing of flow-recirculation zone on the upper-surface.

The flow-separation locations on the base-surface due to the interaction between freestream flow and exhaust plume is affected by the changing of pressure ratio (PR), and the flow-separation locations are determined along the base-surface, as can be seen in Fig.23. The flow-separation locations are determined by measuring the change of the static pressure along the base-surface.

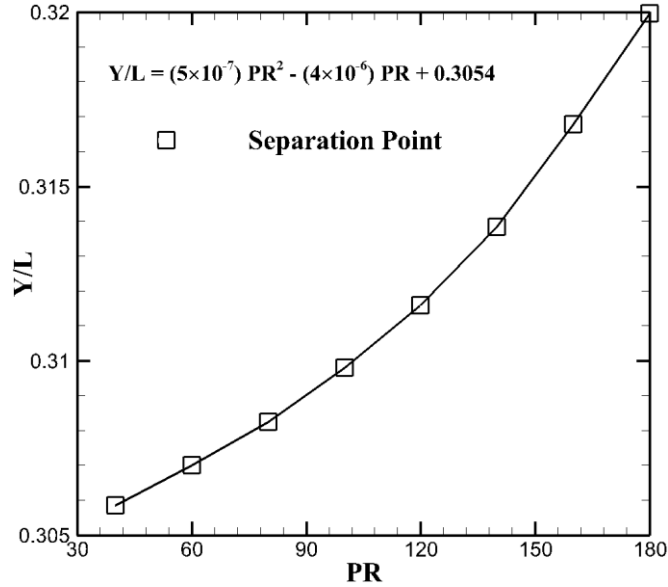


Fig.23 Flow-Separation Locations along the Base-Surface

A trend-line correlation for Fig 5 between the flow-separation locations along the base-surface and the pressure ratio (PR) can be derived in equation (29)

$$Y/L = (5 \times 10^{-7})PR^2 - (4 \times 10^{-6})PR + 0.3054 \quad (29)$$

Equation (29) illustrates the correlation between flow-separation locations along the base-surface with the chamber-to-ambient pressure ratio (PR). When the flow-separation location moves at the edge between upper-surface and base-surface, PIFS starts to happen on the upper-surface, where the corresponding pressure ratio can be calculated by solving equation (29). It can be calculated that when the pressure ratio PR=186, the flow-separation zone will locate at edge between the upper-surface and base-surface when the PIFS starts to occur.

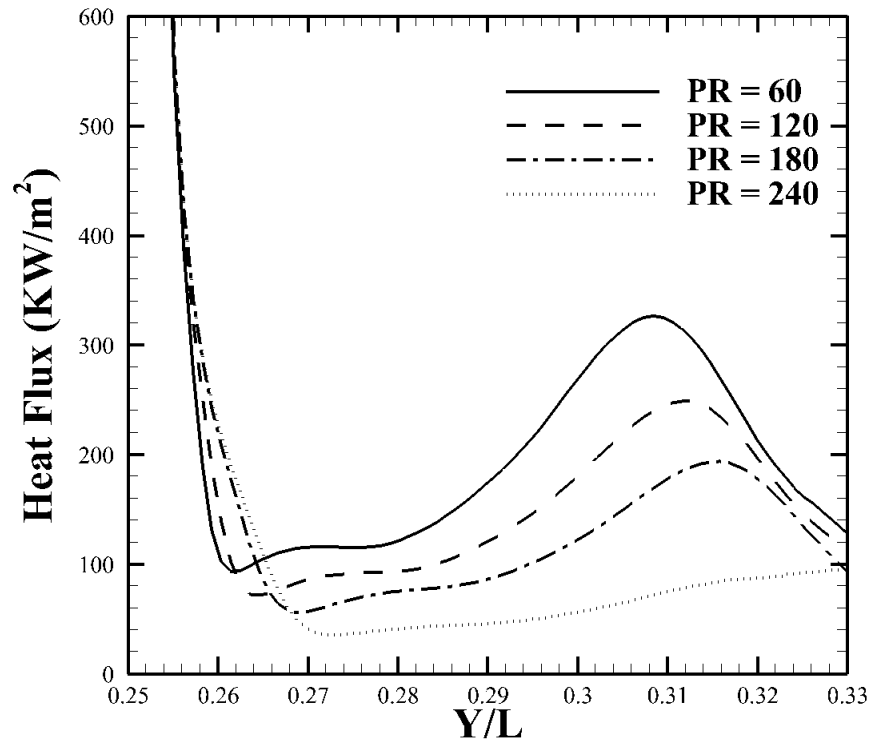


Fig.24 Heat Flux distribution along Base-Surface

The heat flux distribution along the base surface is calculated and plotted under different pressure ratio, as shown in Fig.24. As can be observed in Fig.24, the maximum heat flux point is located at about $Y/L=0.25$, where is the nozzle exit due to the expansion of hot exhaust gas. The base-surface local maximum heat flux points are located at $Y/L=0.31$. As the pressure ratio increases along the base-surface, from $PR=60$ to $PR=240$, the base-surface maximum heat flux decreases while the maximum heat flux point moves upward to the edge between upper-surface and base-surface. When $PR=240$, no obvious local maximum heat flux can be observed along the base-surface, due to the fact that the base-flow/plume interaction almost disappeared on the base-surface and plume induced flow separation (PIFS) starts to happen on the upper-surface.

3.2.2 Effects of Freestream Flow (Ma_∞) on Plume Induced Flow Separation (PIFS)

The effect of freestream Mach number on base-flow/plume interaction and plume induced flow separation (PIFS) were investigated numerically. The parameters considered are

listed in Table 4. The freestream Mach number $Ma_\infty = 1.0$, $Ma_\infty = 1.4$, $Ma_\infty = 2.0$ and $Ma_\infty = 3.2$ were considered. Pressure ratio PR=240 was used and the freestream flow Reynolds number was $Re_\infty = 5.79 \times 10^6$.

Table 4 Baseline Parameters considered for the Freestream Mach (Ma_∞) Effect.

Ma_∞	1.0	1.4	2.0	3.2
PR	240			
Re_∞	5.79×10^6			

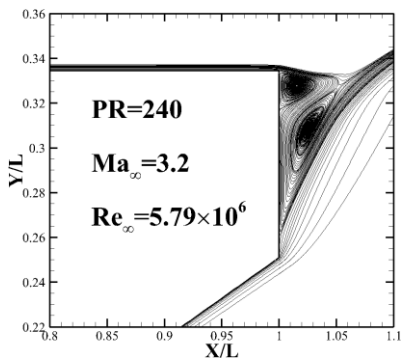
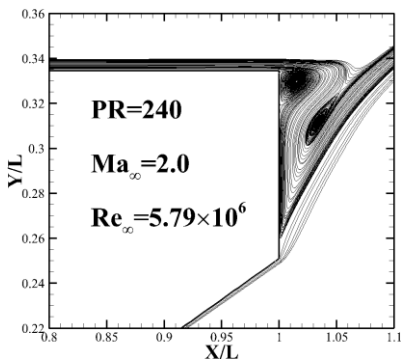
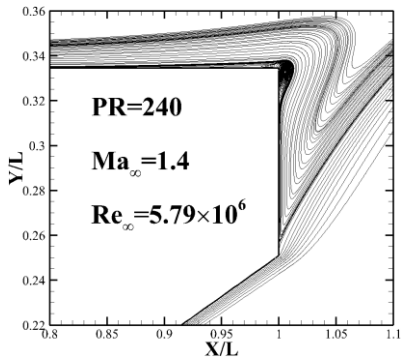
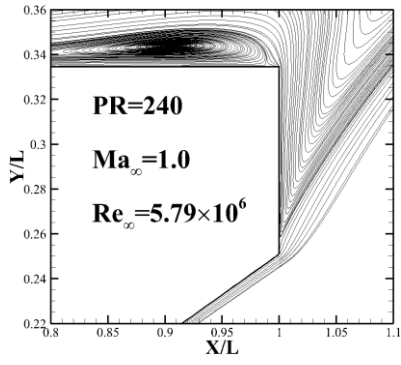


Fig.25 Freestream Flow Condition (Ma_∞) Effect on PIFS and Base-Flow/Plume Interaction

Fig 25 showed the streamline of Ma_∞ effects on PIFS. As can be seen, start with the pressure ratio PR=240 with $Ma_\infty = 1.0$, the PIFS zone can be observed on the upper-surface of the flight vehicle. With the increase of freestream Mach number, from $Ma_\infty = 1.0$ to $Ma_\infty = 1.4$, the PIFS region decreases in size and the location of PIFS zone moves toward the edge between upper-surface and base-surface. With a further increase of freestream Mach number, $Ma_\infty = 2.0$, the PIFS on the upper-surface almost disappeared and the base-flow/plume interaction starts to happen on the base-surface with the flow-recirculation zone being formed. With a further increase of Ma_∞ , $Ma_\infty = 3.2$, one phenomenon can be seen in Fig.25 is that, the flow-separation locations along the base-surface are not changing obviously, which are located at $Y/L = 0.31$. The increasing of freestream Mach number causes the freestream flow carries more kinetic energy, which restricts the expansion of the exhaust plume. Thus, the interaction zone between the freestream flow and the exhaust plume moves toward the base-surface and eventually forms the base-flow/plume interaction. When certain freestream Mach number is reached and forms the base-flow/plume interaction on the base-surface, the flow-recirculation zone is not moving significantly with any further increase of freestream Mach number. Under such conditions, the base-flow/plume separation locations are not changing with the further increase of freestream Mach number, but the heat flux distributions along the base-surface are affected, which can be seen in Fig.26.

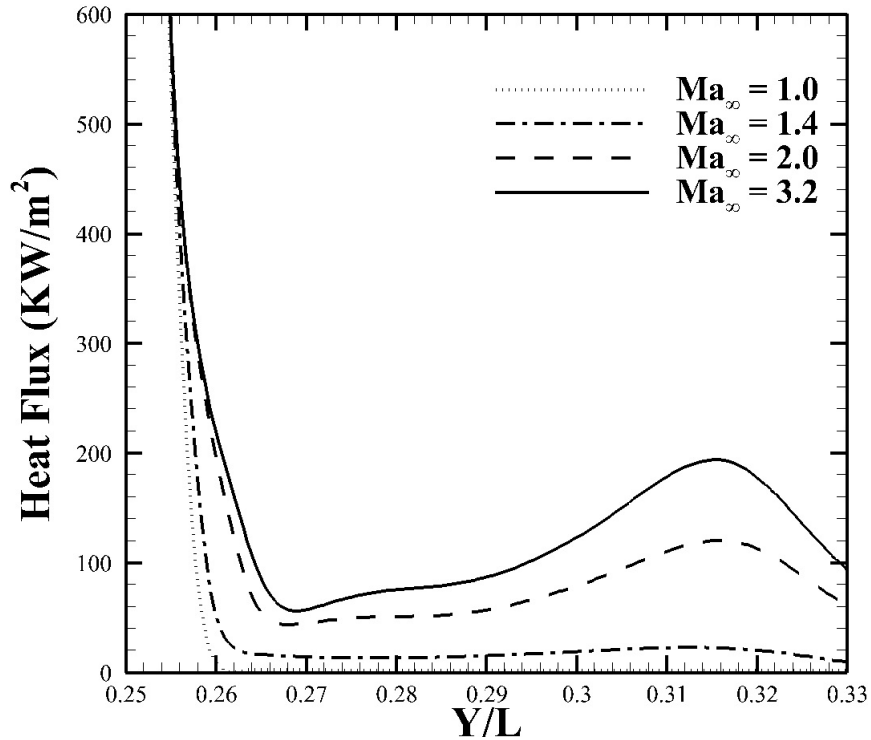


Fig.26 Freestream effects on heat flux distribution along the Base-Surface

As can be observed in Fig.26, the maximum heat flux point is at the nozzle exit, which has been discussed previously. The base-surface local maximum heat flux points are located at $Y/L = 0.32$. As the freestream Mach number along the base-surface increases, from $Ma_{\infty} = 1.0$ to $Ma_{\infty} = 3.2$, the base-surface maximum heat flux increases and the local maximum heat flux locations are not changing obviously. When $Ma_{\infty} = 1.0$, no obvious local maximum heat flux is observed along the base-surface, due to the fact that the base-flow/plume interaction has not started on the base-surface. With further increase of freestream Mach number, $Ma_{\infty} = 2.0$ and $Ma_{\infty} = 3.2$, obvious local maximum heat flux can be observed in Fig.26, because of the formation of base-flow/plume interaction and causes the flow-separation on the base-surface. It can be calculated that the local maximum heat flux for the case with $Ma_{\infty} = 3.2$ is 25 times larger than the case with $Ma_{\infty} = 1.0$ along the base-surface. The plume induced flow separation (PIFS) locations on the upper-surface caused by the changing of freestream Mach number is

plotted in Fig.27. The PIFS locations are calculated by measuring the change of the static pressure along the upper-surface.

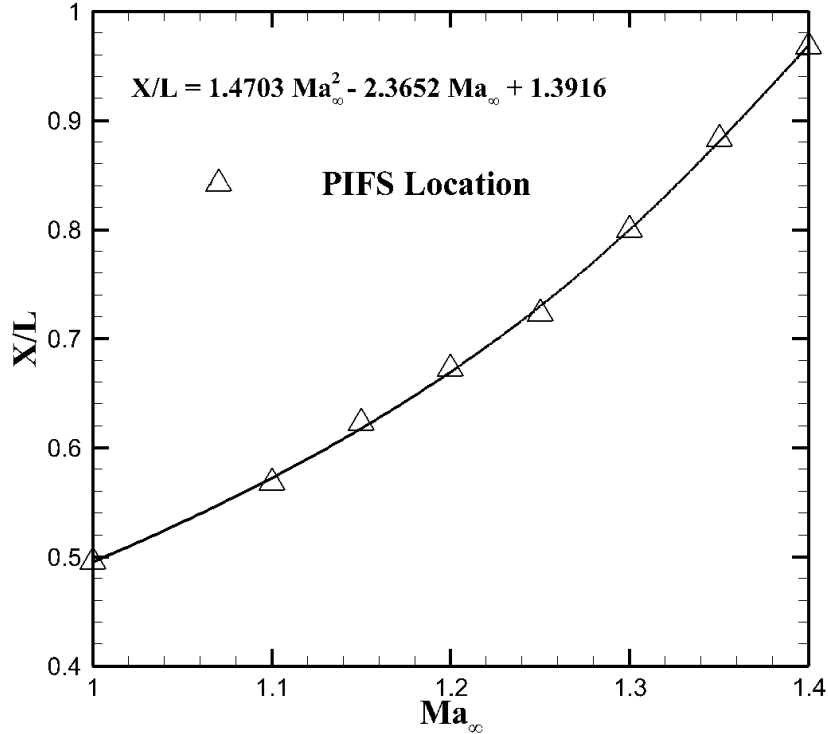


Fig.27 Freestream Effects on PIFS Locations along the Upper-Surface

A trend-line correlation between the PIFS locations and the Ma_{∞} can be derived in equation (30).

$$X/L = 1.4703(Ma_{\infty})^2 - 2.3652(Ma_{\infty}) + 1.3916 \quad (30)$$

As one can see in Fig.27, with the increasing of freestream Mach number, the PIFS first exist on the upper-surface at $X/L = 0.5$, and then it is pushed toward the edge between upper-surface and base-surface, eventually forms the base-flow/plume interaction. It can be calculated from equation (30) that when $Ma_{\infty}=1.42$, the PIFS is located at the edge between the upper-surface

and base-surface, further increase of Ma_∞ causes the disappearance of PIFS on the upper-surface and the formation of the base-flow/plume interaction on the base-surface.

3.2.3 Effect of Geometry Scaling (Re_∞) on Plume Induced Flow Separation (PIFS)

The effect of geometry scaling, reflects as in freestream Reynolds number Re_∞ , on base-flow/plume interaction effect was considered computationally. The parameters considered are listed in Table 5. The freestream Reynolds numbers, $Re_\infty = 5.79 \times 10^5$, $Re_\infty = 2.32 \times 10^6$, $Re_\infty = 5.79 \times 10^6$ and $Re_\infty = 1.16 \times 10^7$ were under consideration. The pressure ratio is kept constant as in PR=240 and the freestream Mach number under consideration is $Ma_\infty = 3.2$.

Table 5 Baseline Parameters considered for the Geometry Scaling (Re_∞) Effect.

Re_∞	5.79×10^5	2.32×10^6	5.79×10^6	1.16×10^7
PR	240			
Ma_∞	3.2			

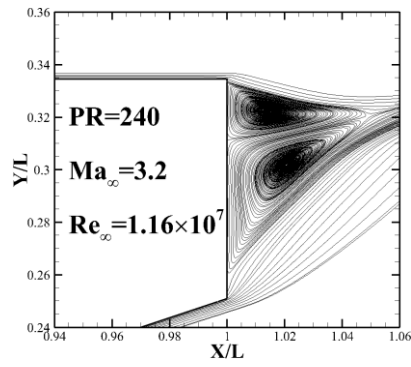
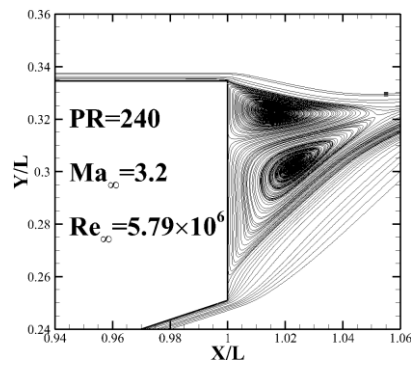
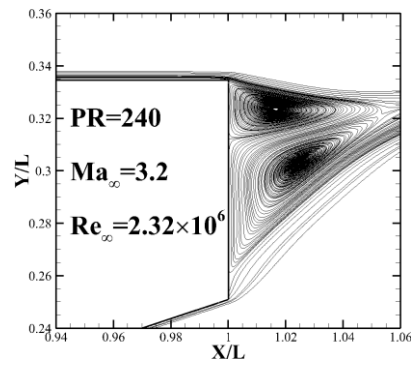
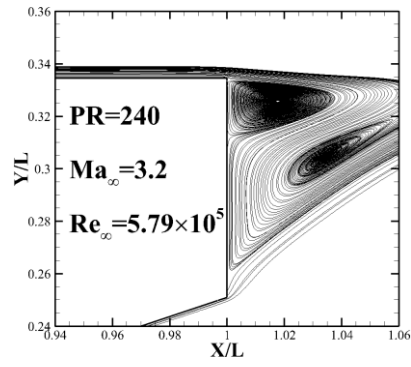


Fig.28 Geometry Scaling (Re_∞) Effects on Base-Flow/Plume Interaction

Fig. 28 shows the streamline of the geometry scaling effects on base-flow/plume interactions. As can be seen in Fig. 28, when the freestream Reynolds number Re_∞ is $\mathcal{O}(10^5)$, the base-flow/plume interaction starts to form on the base-surface, the flow-recirculation as well as the flow-separation phenomenon can be observed. Further increase of Re_∞ , to $\mathcal{O}(10^6)$ and $\mathcal{O}(10^7)$, does not change the flow separation point on the base-surface significantly which is located at $Y/L=0.31$. However, the increase of Re_∞ affected the heat flux distribution along the base-surface, which is calculated and plotted in Fig. 29.

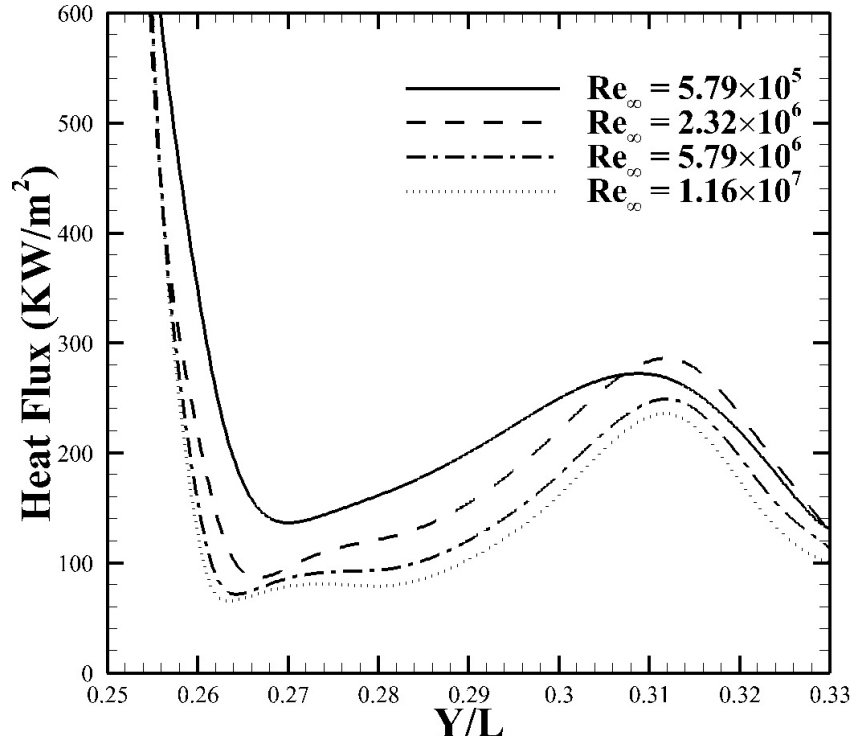


Fig.29 Geometry Scaling (Re_∞) Effects on Heat Flux Distribution along the Base-Surface

It can be seen from Fig. 29 that, the maximum heat flux is located at the nozzle exit, which has been discussed previously. The local maximum heat flux locations on the base-surface, which are located at $Y/L=0.31$. The local maximum heat flux is decreasing with the increasing of Re_∞ . It can be calculated that the local maximum heat flux for the case with $Re_\infty = 5.79 \times 10^5$

is 1.4 times larger than that for the case with $Re_\infty = 1.16 \times 10^7$. As Re_∞ increases, from $Re_\infty = 5.79 \times 10^5$ to $Re_\infty = 1.16 \times 10^7$, the local maximum heat flux locations are not changing obviously on the base-surface, which are located around $Y/L=0.31$.

CHAPTER 4

TRANSIENT ANALYSIS OF PLUME INDUCED SHOCKWAVE AND PLUME INDUCED FLOW SEPARATION ON MINIATURIZED SUPERSONIC NOZZLE

Submitted to *Engineering Application of Computational Fluid Mechanics*, April 2014

This chapter provides a detail description on transient analysis of plume induced shockwave and plume induced flow separation (PIFS) phenomenon on miniaturized nozzles (10^{-2} m to 10^{-3} m) that can be utilized on small-scale flight vehicle. The corresponding parametric studies are carried out in order to obtain a deep understanding of aerodynamics situations that small-scale flight vehicle will face during the flight.

4.1 Computational Schematic and Mathematical Formulation

The schematic diagram of the conical microscale CD nozzle with a smooth throat transition is shown in Fig.30, as well as the plume induced flow separation (PIFS) phenomenon happens on a nozzle with straight afterbody configuration. The design strategy of the nozzle is the same as discussed in Chapter 1 and Chapter 2, follows that outlined in Liu et al. [86] The half-angle of the divergent region of the nozzle for all cases was held constant ($\theta = 15^\circ$) and the designed nozzle exit Mach number is 3.0.

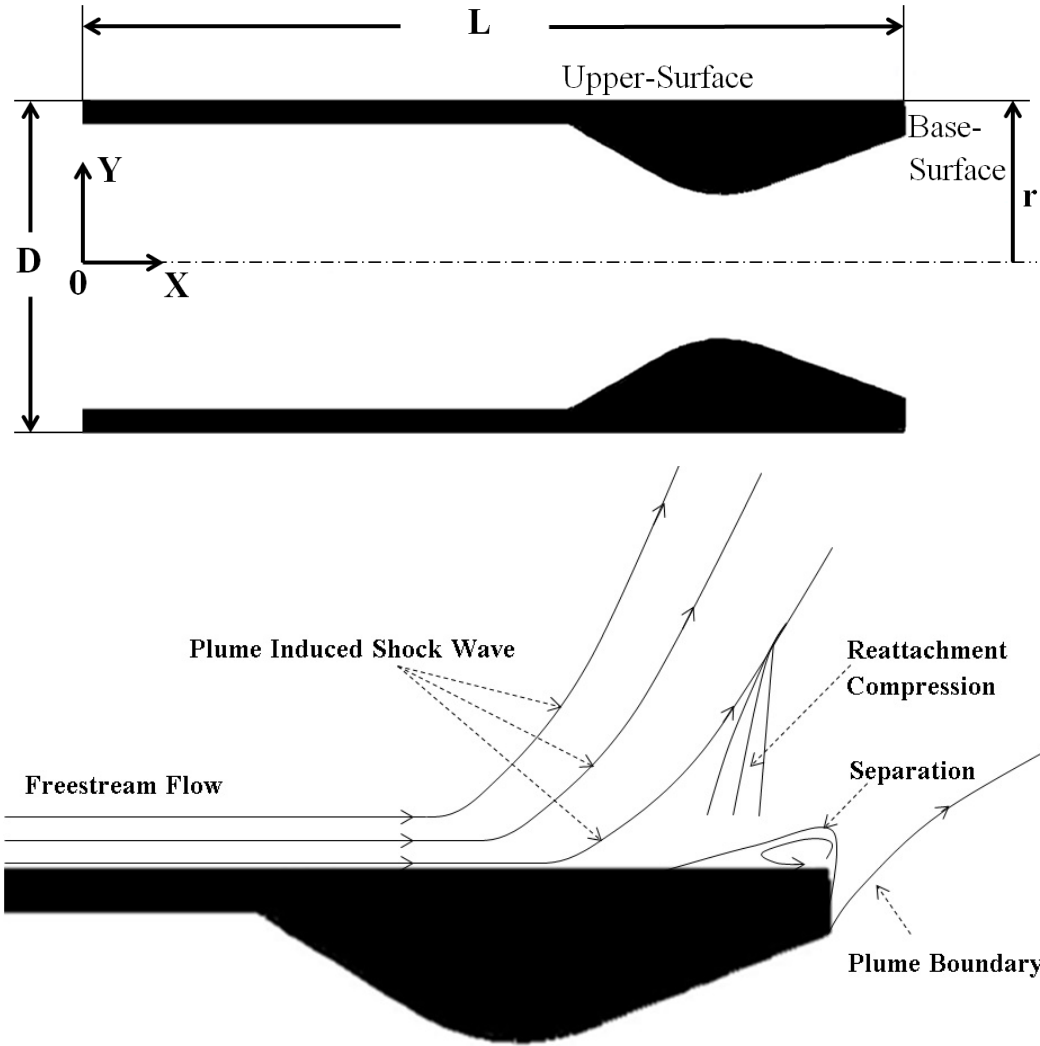


Fig.30 Plume-Freestream interference schematic

The governing equation solved for PIFS phenomenon, is used the same as in Chapter 2, from equation (19) to (24), the axisymmetric form of compressible continuity, Navier-Stokes, and energy equations.

The thermo physical properties of specific heat and dynamic viscosity were respectively modeled using a fifth order polynomial [123] and the power law [124]. The pressure inlet boundary condition was specified at the inlet flow and the pressure outlet boundary condition was used at the outlet flow. The nozzle wall was set as in adiabatic, no-slip boundary condition. A 2-equation $k - \epsilon$ Re-Normalization Group (RNG) model [131] was used for turbulence

calculations. The turbulent viscosity is calculated as in equation (31), where k is the turbulent kinetic energy and ϵ is the dissipation rate. The model constants $C_\mu = 0.0845$, $C_{1\epsilon} = 1.42$, $C_{2\epsilon} = 1.68$ are used.

$$\mu_t = \rho C_\mu (k^2 / \epsilon) \quad (31)$$

4.1.1 Numerical Method

The governing equations were solved by using the commercially available CFD package ANSYS-FLUENT version 13.0. A structured grid was generated using ANSYS Workbench. The computational domain is shown in Fig.31, and the computational domain outside the nozzle has been truncated in the figure. The entire computational domain is not shown in the figure so that a more detailed representation of the computational grid within the nozzle may be presented.

The pressure inlet boundary condition was applied to the nozzle inlet, where the total and static pressure can be specified, and the isentropic relations are utilized to evaluate the velocity magnitude at the boundary. The nozzle wall was set as in adiabatic, no-slip boundary condition, where the normal and tangential velocity components at the wall are identically zero and the temperature gradient on the wall is zero for the corresponding boundary. The boundary condition for the external computational domain of the nozzle was set as in pressure far field, under such condition, the freestream Mach number and the ambient pressure can be specified of the external flowfield, and the density is calculated by using ideal-gas law for such boundary condition.

Density-velocity coupling, for the above mentioned governing equations and boundary conditions, was achieved using a coupled implicit solver [127]. A second-order upwind scheme [128] was used to discretize advective terms. The transient computational results are second-order accurate in time with a step size $\Delta t = 10^{-4}$ second.

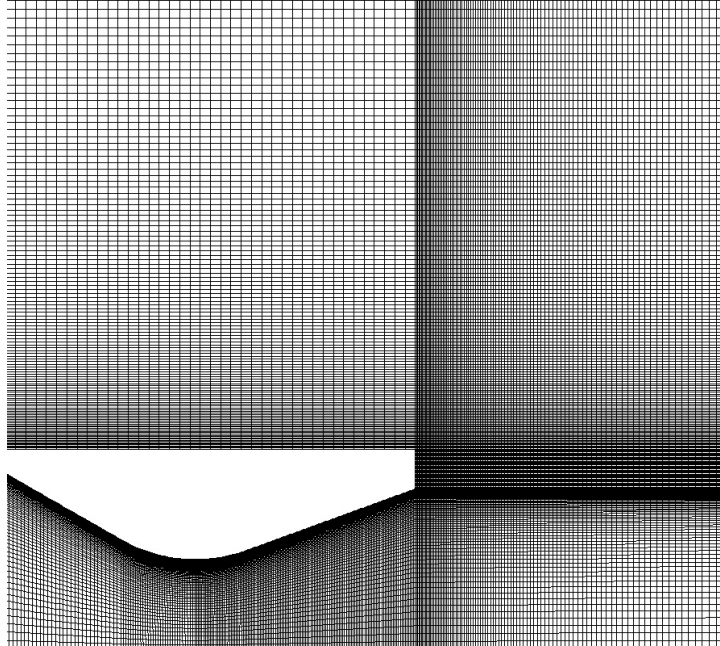


Fig.31 Computational domain

4.1.2 Verification & Validation

The study of grid independent was conducted. The static-to-ambient pressure ratio profile (P/P_{∞}) along the nozzle upper-surface was used to determine grid independence. Initially, a computational domain with 20,000 cells with a step size $\Delta t = 10^{-2}$ was used to calculate the pressure ratio profile. The verification of the computational grid was done by increasing the number of cells as well as the time step size in the computational domain until the calculated pressure profile was within 1% of each other. Using this criterion, it was determined that a computational domain with 98,000 cells and time step size with $\Delta t = 10^{-4}$ was sufficient to produce grid independent results.

The computational results were validated by comparison with the computational and experimental results of Lee [105], as can be seen from Fig. 32. It was calculated that the maximum deviation from Lee's experimental data was 5.45%. Thus, the current computational model may be considered valid.

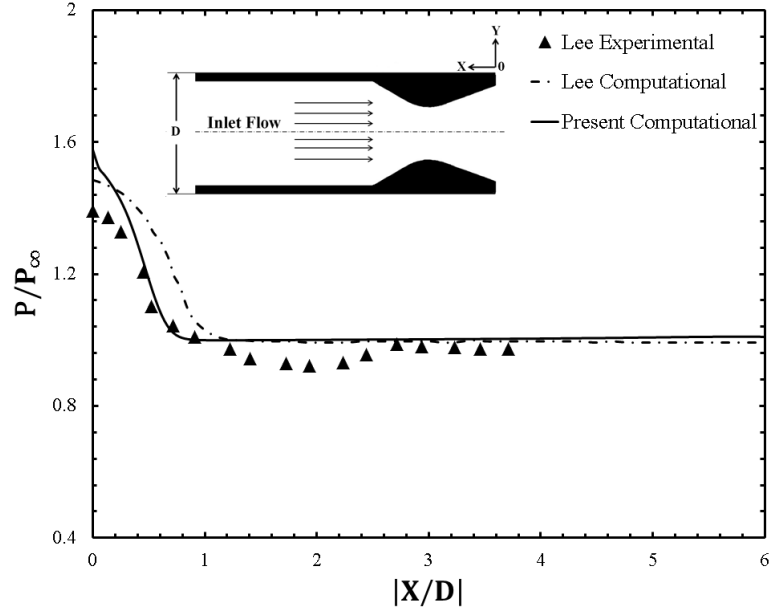


Fig.32 Validation of computational model

4.2 Results & Discussion

4.2.1 Effects of Pressure Ratio (PR) on Plume Induced Shockwave and PIFS

The variables under consideration are listed in Table 6. The pressure ratios PR=40, PR=103.5, PR=247.5 and PR=539.6 were utilized, and the freestream Mach number $Ma_\infty = 1.5$ was kept as constant. The change of the pressure ratio along with the change of altitude under considerations follows the Barometric formula [132], which is described in equation (32-33).

Table 6 Baseline Variables considered for the Pressure Ratio (PR) Effect.

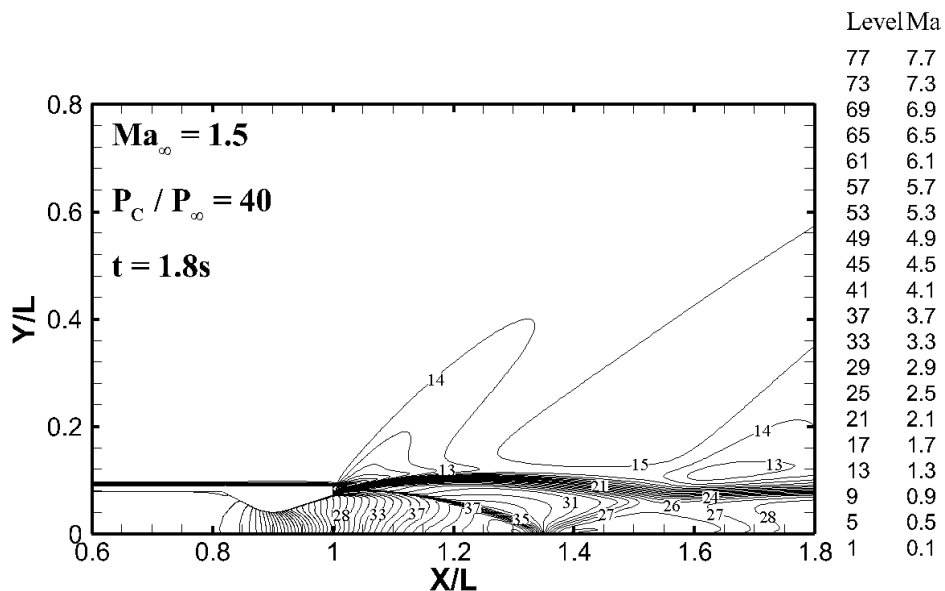
PR	40	103.5	247.5	539.6
Ma_∞	1.5	1.5	1.5	1.5

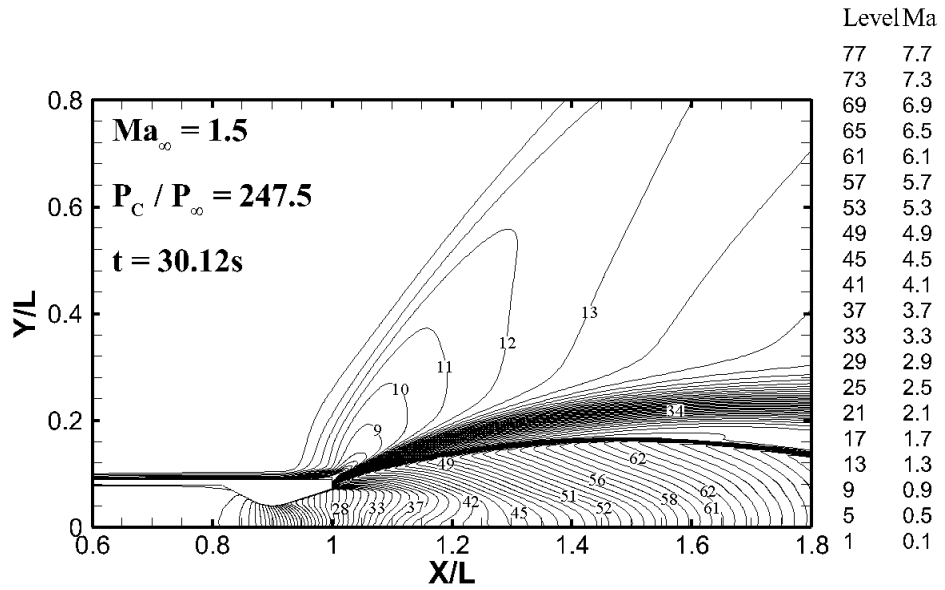
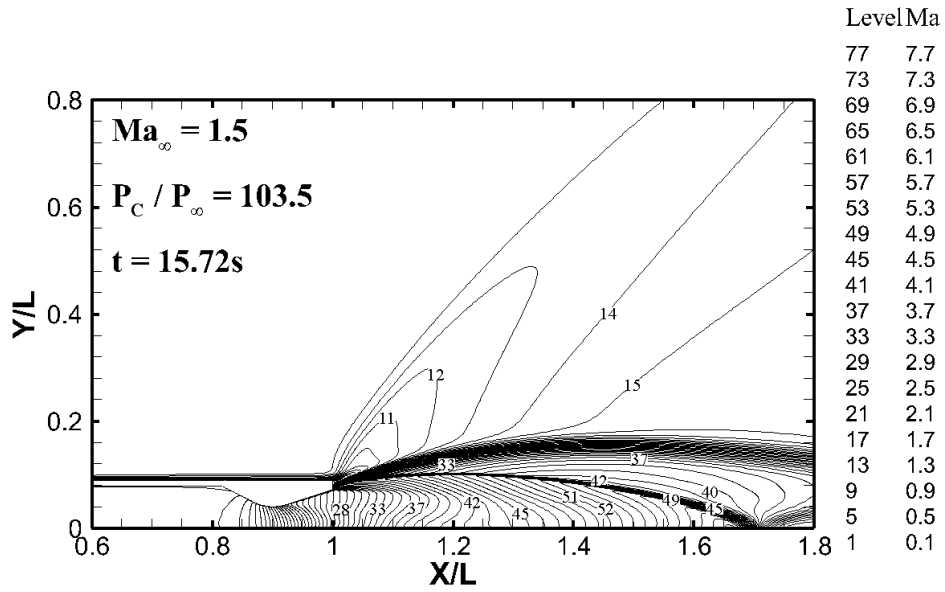
$$P = P_\infty e^{(-Mg_0 h)/(RT)} \tag{32}$$

where

$$h = Ma_\infty \sqrt{\gamma RT} t \tag{33}$$

Fig.33 shows the Mach contour under different pressure ratios. As can be observed in Fig.33, under the pressure ratio $PR=40$, the plume induced shockwave is formed on the upper-surface. As the pressure ratio increases, from $PR=103.5$ to $PR=247.5$, the plume induced shockwave moves along the upper-surface toward the leading-section of the flight vehicle. With a further increase of pressure ratio, $PR=539.6$, an obvious further expansion of plume can be observed, the plume induced shockwave is moving further forward to the leading-section along the upper-surface. With the increase of the altitude, the ambient pressure decreases due to the density decrease of the air, the pressure ratio between the nozzle chamber and ambient increases, this results the size expansion of exhaust plume. When the freestream flow interacts with the exhaust plume, the shockwave is formed on the upper-surface due to the rapid change of the pressure [130]. With the increase of the pressure ratio, the exhaust plume experiences a further expansion in size, as such, the interaction between the freestream flow and the plume moved toward the leading-section on the upper-surface and results in the corresponding motion of plume induced shockwave.





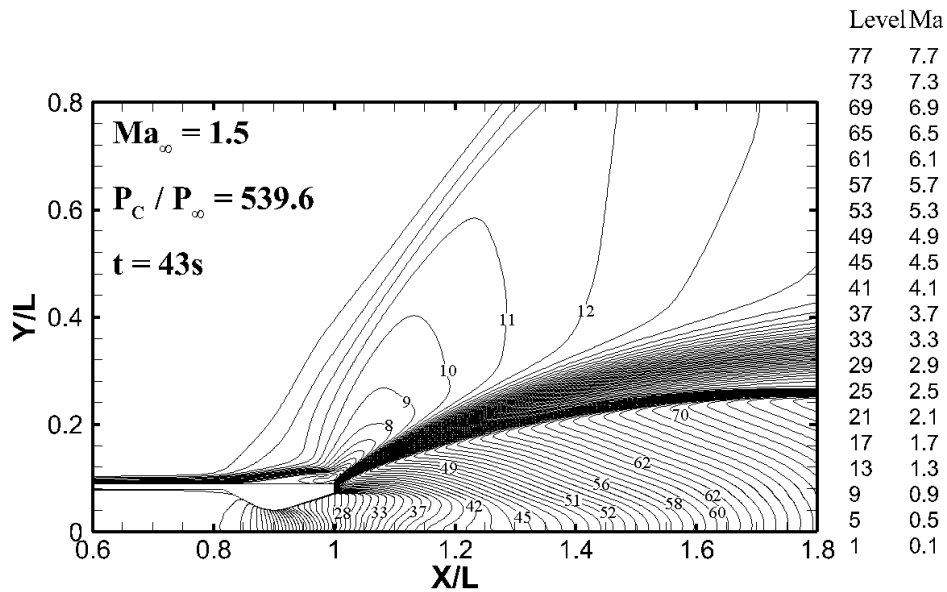


Fig.33 P_c/P_∞ pressure ratio effects on plume induced shockwave

The plume induced shockwave locations were shown in Fig.34. The location was determined by measuring the change of static pressure along the upper-surface. As can be seen, the increase of the chamber to plume pressure ratio caused the plume induced shockwave locations moves from $X/L = 1$ to $X/L = 0.79$.

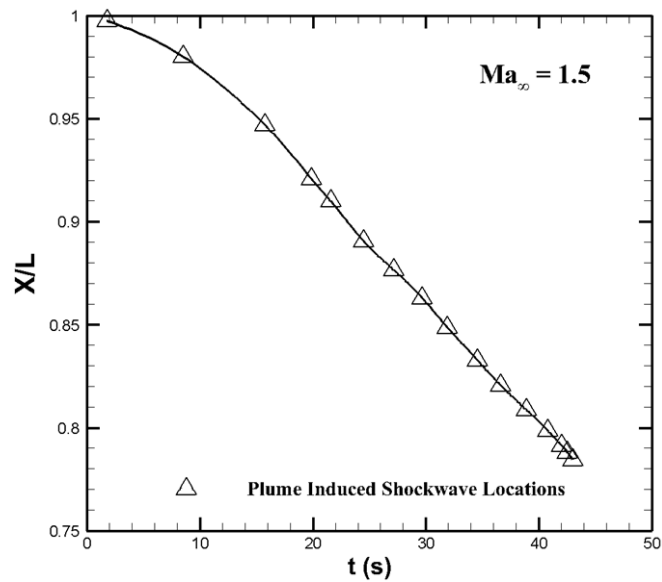
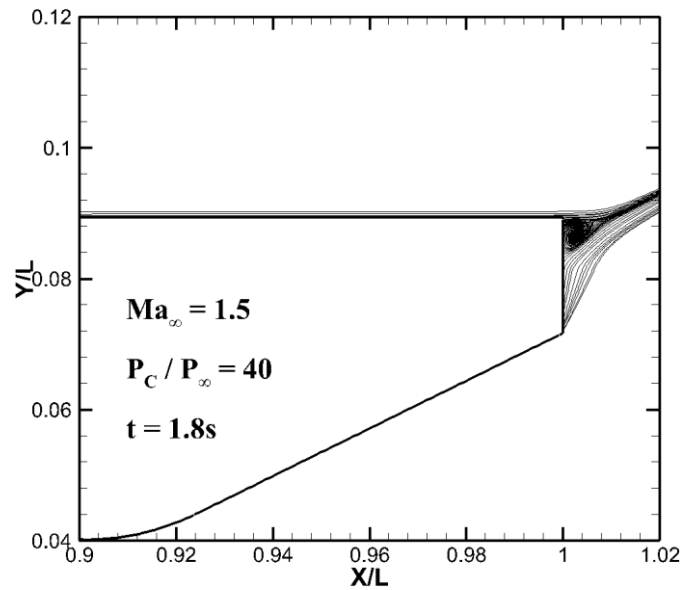


Fig.34 Plume Induced Shockwave Locations affected by Pressure Ratio (PR)

A correlation can be derived as shown in equation (34) to describe the motion of plume induced shockwave locations with the change of time as in

$$X/L = -3 \times 10^{-5} t^2 - 0.0041 t + 1.0117 \quad (34)$$

The plume induced flow separation (PIFS) phenomenon caused by the plume-freestream flowfield interaction, as can be observed in Fig.35. The interaction between the freestream flow and the exhaust plume results in the formation of flow-recirculation zone on the base-surface and upper-surface, due to the existence of adverse pressure gradient in the interaction zone with the increasing of the pressure ratio (PR), the flow-recirculation zone is formed on the base-surface first, and eventually moves toward the upper-surface of the flight vehicle with a further increase of the pressure ratio and results in the flow separation.



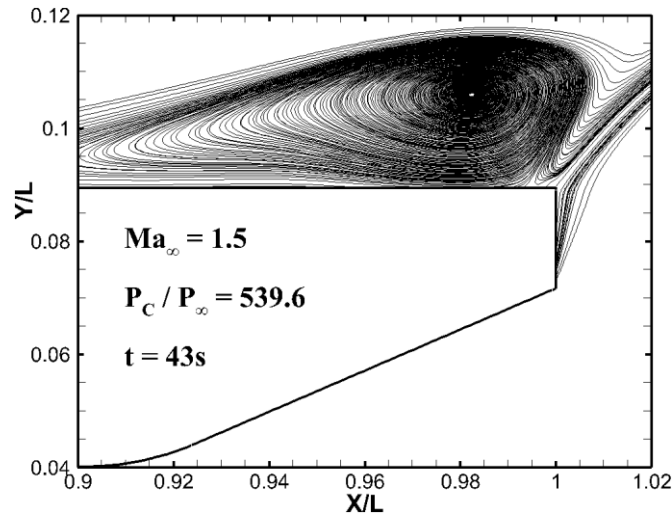


Fig.35 Plume Induced Flow Separation (PIFS) affected by the Pressure Ratio (PR)

Fig.35 shows the base-flow/plume interaction and PIFS phenomenon under the pressure ratio PR=40 and PR=539.6. As can be seen, with the further expansion of the exhaust plume due to the increasing of the pressure ratio, the flow-recirculation zone is formed on the upper-surface and expands more in size. The formation of flow-recirculation zone generates the locally overheating zone, the “hot zone”, on the surface of the flight vehicle due to the occurring of convective heat transfer. Fig.36 shows the “hot zone” temperature profile and the locations of the “hot zone” under different times on the base-surface.

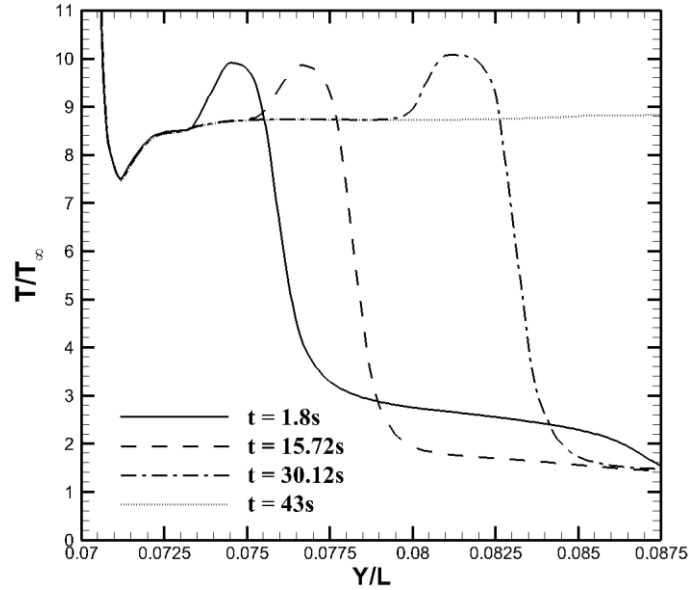


Fig.36 “Hot Zone” along the base-surface affected by Pressure Ratio (PR)

It can be seen from Fig.36, the maximum T/T_{∞} is located at $Y/L = 0.071$, where the nozzle exit is located due to the rapid expansion of hot exhaust plume. It can be calculated that in the “hot zone”, the local maximum temperature is 10 times higher than the ambient temperature along the base-surface. Also, the “hot zone” is moving from the base-surface toward the upper-surface due to the expansion of exhaust plume. When the time $t=1.8s$ with the corresponding pressure ratio $PR=40$, the base-flow/plume interaction on the base-surface is formed and leads the formation of flow-recirculation zone, which results in the formation of “hot zone”. With a further increase of time, $t=15.72$ with the pressure ratio $PR=539.6$, no local maximum temperature ratio is observed, due to the reason that the exhaust plume expand more with the increase of pressure ratio, and forms the plume induced flow separation (PIFS) on the upper-surface of flight vehicle, the base-flow/plume interaction on base-surface almost disappears and the “hot zone” moves from base-surface to upper-surface.

4.2.2 Effects of Freestream Flow (Ma_∞) on Plume Induced Shockwave and PIFS

The variables under consideration are listed in Table 7. The chamber-to-ambient pressure ratio, $PR=160$, was kept constant for all cases. The freestream flow $Ma_\infty = 1.5$, $Ma_\infty = 2.29$, $Ma_\infty = 3.0$ and $Ma_\infty = 3.65$ were considered.

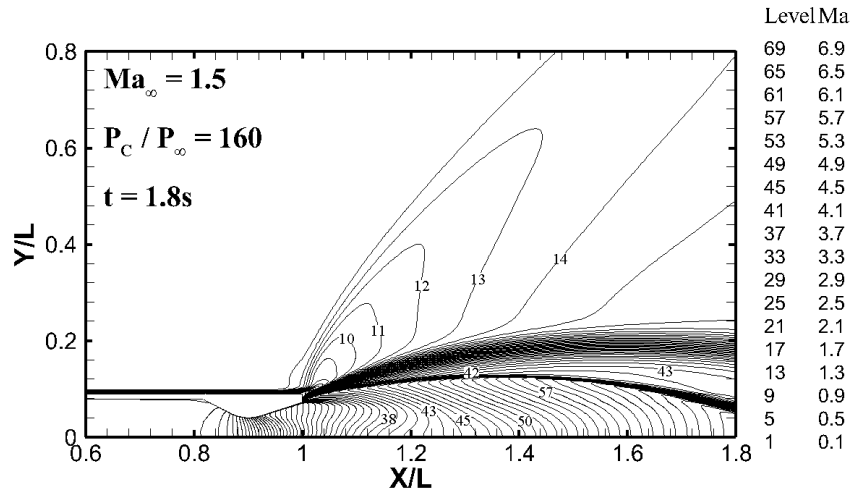
Table 7 Baseline Variables considered for the Freestream Flow (Ma_∞) Effect.

Ma_∞	1.5	2.29	3.0	3.65
PR	160	160	160	160

The freestream Mach number is varied linearly by assuming the flight vehicle has a constant acceleration process, as described in Equation (35).

$$Ma_\infty = 1.5 + 0.05t \quad (35)$$

Fig.37 shows the Mach contour of freestream flow effects on plume induced shockwave.



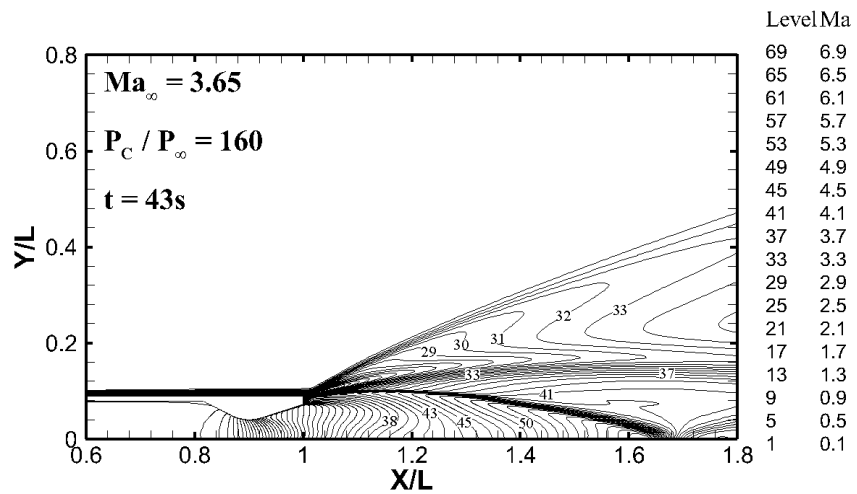
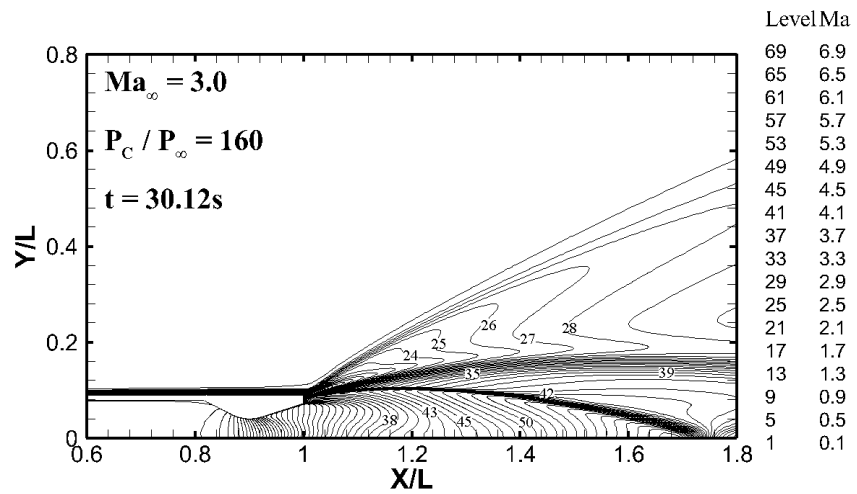
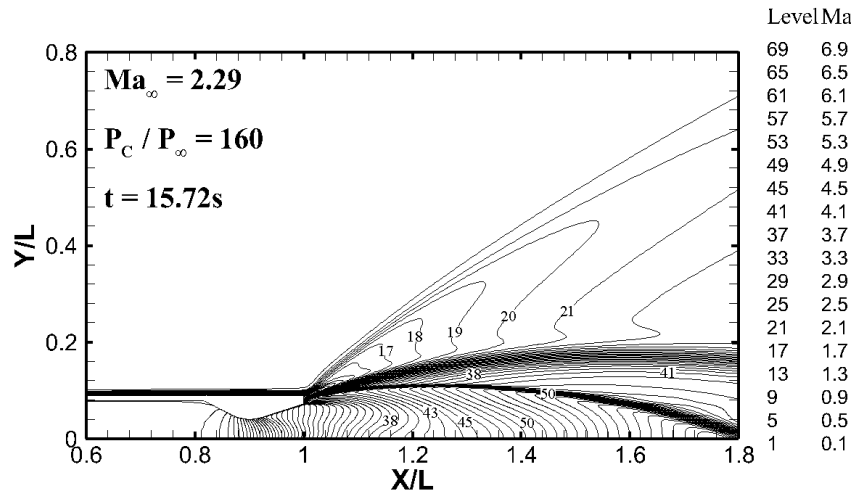


Fig.37 Freestream Mach number effects on plume induced shockwave

As can be observed in Fig.37, with the increasing of freestream Mach number, from $Ma_\infty = 1.5$ to $Ma_\infty = 2.29$, the location of plumed induced shockwave moves along the upper-surface, and the expansion size of the exhaust plume decreased. Due to the fact that the increase of the Ma_∞ causes the freestream flow carries more kinetic energy, which will restrict the expansion of the exhaust plume. As such, a size decreasing of plume size is observed as well as the motion of the plume induced shockwave along the upper-surface. With a further increase of freestream Mach number, $Ma_\infty = 3.0$ and $Ma_\infty = 3.65$, the plume induced shockwave locate at $X/L = 0.983$ on the upper-surface of the flight vehicle, and no obvious further movement of this location is observed.

The plume induced shockwave locations were shown in Fig.38. The location is determined by measuring the change of static pressure along the upper-surface. As can be seen, when the time changed from $t=1.8s$ to $t=20s$, with the corresponding freestream Mach number varied from $Ma_\infty = 1.5$ to $Ma_\infty = 2.43$, the location of plume induced shockwave is moving along on the upper-surface of the flight vehicle from $X/L = 0.91$ to $X/L = 0.98$. Any further increase of the time, from $t=20s$ to $t=43s$, with freestream Mach number from $Ma_\infty = 2.6$ to $Ma_\infty = 3.65$, do not change the location of plume induced shockwave obviously, which located at $X/L = 0.98$. A trend line correlation can be derived as shown in equation (36) to describe the motion of plume induced shockwave locations with the change of time. From equation (36), it can be calculated that once the flow time reaches $t=20s$, any further increase of time does not change the plume induced shockwave locations obviously.

$$\begin{cases} X/L = -0.0001t^2 + 0.068t + 0.8995 & t \in [1.8s, 20s] \\ X/L = 0.0002t + 0.9809 & t \in [20s, 43s] \end{cases} \quad (36)$$

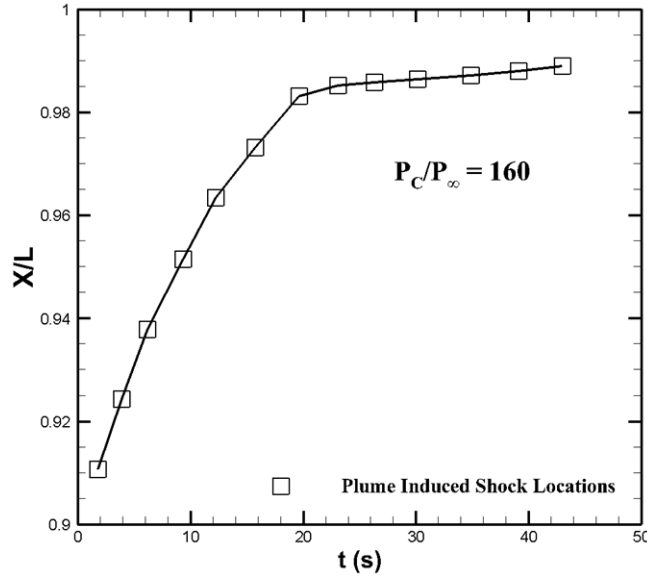
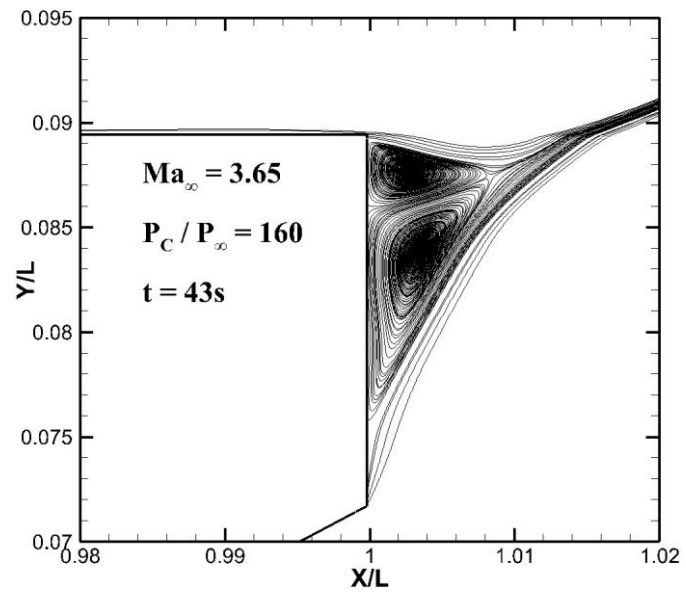
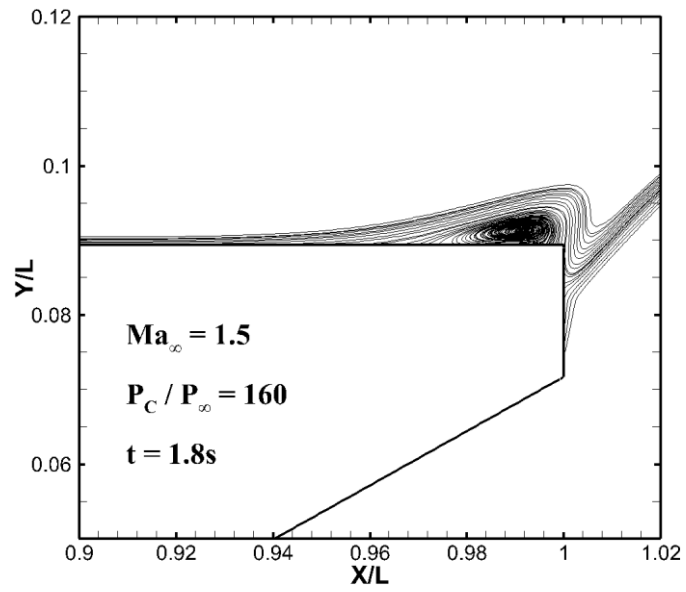


Fig.38 Plume induced shockwave locations affected by freestream Mach number

Fig.39 shows the base-surface/plume interaction phenomenon affected by the freestream flow. As can be observed in, under a constant pressure ratio, $PR=160$, when $Ma_\infty = 1.5$, the PIFS first started on the upper-surface of the flight vehicle. With the increase of freestream Mach number, $Ma_\infty = 3.65$, the freestream flow carries more kinetic energy and causes the movement of PIFS from the upper-surface toward the base-surface and results in the base/flow-plume interaction. By measuring the change of static pressure along the base-surface, it can be calculated that the base-flow/plume separation point located at $Y/L = 0.087$ on the base-surface. Any further increase of freestream Mach number, from $Ma_\infty = 3.65$ to $Ma_\infty = 5.2$, this flow-separation location does not change significantly.



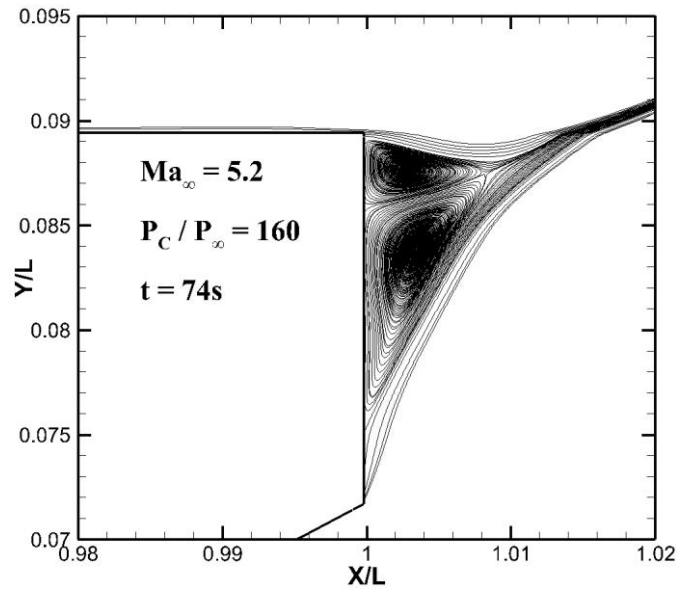


Fig.39 Base-Surface/Plume interaction affected by the freestream Mach number

The freestream Mach number effect on temperature distribution along the base-surface is plotted and can be seen in Fig.40.

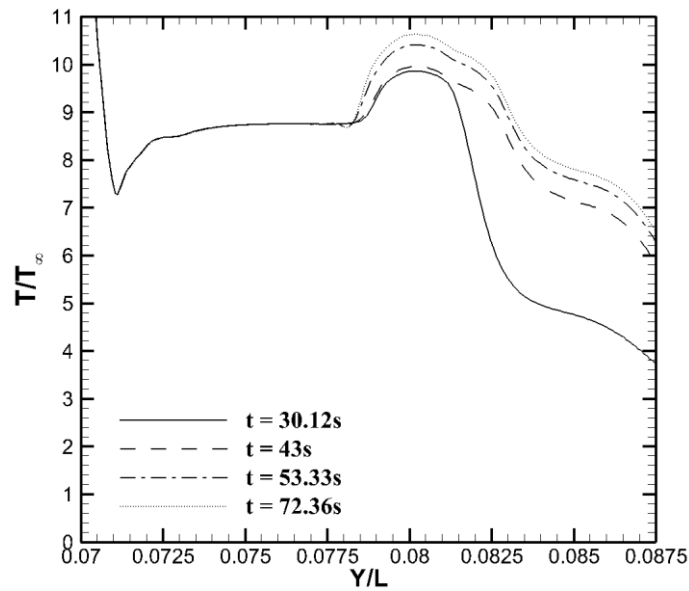


Fig.40 “Hot Zone” along the base-surface affected by the Freestream Flow (Ma_∞)

As discussed before, the base-flow/plume interaction forms the flow-recirculation zone and causes the locally overheating zone, the “hot zone”, along the base-surface. The “hot zone” distribution affected by the freestream Mach number varied with time is shown in Fig.40. As can be observed, the maximum temperature ratio is located at $Y/L = 0.071$, where the nozzle exit is located due to the rapid expansion of hot exhaust plume, as discussed previously. It can be calculated that for the “hot zone”, the local maximum temperature T along the base-surface is 10 times compare to that of the ambient temperature T_∞ , and the “hot zone” location, which locates at $Y/L = 0.08$, does not move obviously with further increase of flow time, from $t=30.12s$ to $t=72.36s$ with the corresponding freestream Mach number varied from $Ma_\infty = 3.0$ to $Ma_\infty = 5.2$. However, the further increase of Ma_∞ affects the local maximum temperature distribution. It can be calculated that for $t=72.36s$ with $Ma_\infty = 5.2$, the local maximum temperature ratio T/T_∞ is 1.5 times higher than that with $t=30.12s$ with $Ma_\infty = 3.0$, due to the fact that the freestream flow with higher Mach number carries more kinetic energy compared to that with lower Mach number.

CHAPTER 5 CONCLUSIONS

This chapter provides the conclusions of computational modeling on microscale and miniaturized converging-diverging nozzle. The “Saw Tooth” surface modification effects of reducing viscous forces on microscale CD nozzle as well as the aerodynamics analyses of plume induced shockwave and plume induced flow separation on CD nozzle are concluded.

5.1 Conclusion of “Saw Tooth” Surface Modification on Microscale CD Nozzle

The cold-gas micronozzle was studied numerically. It is a known fact that the viscous effects will affect the microscale nozzle performance due to the small sizing. A “Saw Tooth” nozzle wall configuration was implemented in order to reduce the viscous effects and improve the nozzle performances. The right triangle with tooth angle α was used to simulate the “Saw Tooth” nozzle wall.

- Five numerical cases with the nozzle throat radius, $R_t = 80 \mu m$, $R_t = 60 \mu m$, $R_t = 50 \mu m$, $R_t = 40 \mu m$ and $R_t = 30 \mu m$ were studied to illustrate the viscous effects caused by geometry scaling. Results showed due to the viscous effects because of decreasing geometry size, the thrust coefficient (C_f) decrease by about 2.13%, the specific impulse efficiency ($I_{sp}/I_{sp-inviscid}$) decrease by about 1.11%, the exit Mach number decreased by about 2.38% and the viscous obstructed up to 4% of the nozzle exit area.

- Four cases with the “Saw Tooth” nozzle wall configurations were investigated numerically. The number of tooth varied from $N = 10$ to $N = 60$. The results showed that with cases when N was above 40, the flow field became stable and no obvious deviation was indicated from the

inviscid flow case. Vortices were observed inside the saw tooth, and an increasing number of N resulted an increasing of nozzle performance. The results showed that when the number of tooth varied from $N = 0$ to $N = 60$, the thrust coefficient (C_f) and the specific impulse efficiency ($I_{sp}/I_{sp-inviscid}$) increase by up to about 0.83%.

- The effect of different tooth angles were investigated by considering $\alpha = 15^\circ$, $\alpha = 25^\circ$ and $\alpha = 30^\circ$. An increasing of nozzle performance was indicated by increasing α . Results showed that thrust coefficient (C_f) and the specific impulse efficiency ($I_{sp}/I_{sp-inviscid}$) increase by up to 0.9% by varying the fin angle from $\alpha = 15^\circ$ to $\alpha = 30^\circ$ for the case with number of saw tooth $N = 60$.

5.2 Conclusions on the Analysis of PIFS on CD Nozzle

The computational study was conducted to analyze the base-flow/plume interaction at the base-surface and plume induced flow separation (PIFS) at the upper-surface of miniaturized flight vehicle. The effects of chamber-to-ambient pressure ratio (PR), freestream flow conditions (Ma_∞) as well as geometry scaling effects (Re_∞) were considered and investigated numerically. The separation point along the base-surface and the PIFS location at the upper-surface were determined, the heat flux distribution along the base-surface was also considered.

- Several numerical cases were carried out in order to analyze the pressure ratio effect on PIFS and base-flow/plume interaction. The pressure ratio (PR) under consideration ranged from PR=60 to PR=240. At lower PR (PR=60), there existed the base-flow/plume interaction and formed the flow-recirculation zone along the base-surface; further increase of PR pushed the flow-separation region toward the upper-surface as well as decrease the size of flow-recirculation zone. When the PR reaches about PR=180, the flow-recirculation zone at the base-surface almost disappeared and further increase of PR resulted the PIFS at the upper-surface. A correlation was

derived to investigate the PR effects on the flow-separation point along the base surface. The heat flux distribution along the base-surface was also considered, which illustrated the change of heat flux along the base-surface with the change of PR.

- The effects of freestream Mach number on base-flow/plume interaction and PIFS were studied numerically. The freestream Mach number varied from $Ma_\infty = 1.0$ to $Ma_\infty = 3.2$ were considered. When $Ma_\infty = 1.0$, the PIFS was formed at upper-surface; with a further increase of the Ma_∞ the flow separation was pushed toward the tail-section edge of the upper-surface. When the freestream Mach number reached about 1.4, the PIFS at the upper-surface disappeared and the base-flow/plume started at the base-surface. Once the base-flow/plume interaction started at the base-surface, any further increase of Ma_∞ did not change the flow-separation point locations but made the flow-recirculation zone more obvious to be observed. A correlation was derived by considering Ma_∞ and the PIFS location along the upper-surface. The heat flux distribution along the base-surface was calculated to illustrate the Ma_∞ effects on the base-surface.

- Different computational cases were conducted to investigate on the geometry scaling effects on the PIFS and base-flow/plume interaction. The freestream Reynolds number, Re_∞ was used to reflect the geometry scaling factor. The freestream Reynolds number under consideration ranged from $Re_\infty = 5.79 \times 10^5$ to $Re_\infty = 1.16 \times 10^7$. When the Re_∞ was in the order of 10^5 , base-flow/plume interaction started at the base-surface with the flow-recirculation zone. Further increase of the Re_∞ made the base-flow/plume interaction phenomenon more obvious to be observed, but the flow-separation point was not changing obviously for the flow-recirculation zone along the base-surface. The heat flux distribution along the base-surface with different Re_∞ were calculated and plotted to show the geometry scaling effects on heat flux distribution along the base-surface.

5.3 Conclusion on the Transient Analysis of CD Nozzle

The transient computational studies were conducted to analyze the plume induced shockwave and the plume induced flow separation (PIFS) phenomenon. The effects of chamber-to-plume pressure ratio (P_c/P_∞) and freestream Mach number (Ma_∞) were considered and investigated numerically. The plume induced shockwave locations that varied with the pressure ratio (P_c/P_∞) and the freestream Mach number (Ma_∞) were determined. The plume induced flow separation (PIFS) between freestream and the exhaust plume were studied, and the local “hot zone” (T/T_∞) were calculated and plotted along the base-surface of the flight vehicle.

- The plume induced shockwave locations were found to be moved toward the leading-section on the upper-surface by increasing the pressure ratio P_c/P_∞ . A correlation was derived to describe the movement of plume induced shockwave.
- The increasing of the pressure ratio (PR) caused the flow separation between the exhaust plume and the freestream flow, and resulted in the flow-recirculation zone, which caused the formation and movement of “hot zone”, from the base-surface toward the upper-surface. The locations of the “hot zone” were calculated and plotted on the base-surface, and the “hot zone” temperature was calculated to be 10 times higher than that of the freestream temperature.
- The increasing of the Ma_∞ caused the movement of plume induced shockwave along the upper-surface. The locations of plume induced shockwave affected by freestream Mach number were determined. A correlation was derived to describe the plume induced shockwave locations.
- The freestream Mach number effect on plume induced flow separation was studied computationally. The increase of the Ma_∞ caused the movement of PIFS on the upper-surface toward the base-surface, which resulted the base-flow/plume interaction and flow-separation. It was calculated that the “hot zone” maximum temperature was 10 times larger than that of ambient

temperature T_∞ , and the local maximum temperature ratio T/T_∞ was 1.5 time larger for the case with a higher freestream Mach number, $Ma_\infty = 5.2$ than that with a lower freestream Mach number, $Ma_\infty = 3.0$.

REFERENCES

- [1] Neilson, R., "The Steam Turbines: Science, Technology, and the Parsons Family", Taylor & Francis Group, New York, 1903
- [2] Stevens, T. and Hobart, H.M., "Steam Turbine Engineering", MacMillan CO., New York, 1906
- [3] Hunley, J.D., "Technology and Culture", Johns Hopkins University Press, Vol.36, No.2, pp.327-350, 1995
- [4] Shapiro, A.H., "The Dynamics and Thermodynamics of Compressible Fluid Flow", Vol.1 & 2, Ronald Press CO., New York, 1953
- [5] Sutton, G.P., "Rocket Propulsion Elements", 6th Edition, John Wiley & Sons, Inc., NY, 1992
- [6] Grisnik, S.P and Smith, T.A., "Experimental Study of Low Reynolds Number Nozzles", NASA TM-89858, May 1987
- [7] Humble, R.W., Henry, G.N., and Larson, W.J., "Space Propulsion Analysis and Design", McGraw-Hill Companies, Inc., 2nd edition, New York, 1995
- [8] Cardin, J.M. and Mosher, L.E., "A Low Power Approach to Small Satellite Propulsion", 13th AIAA/USU Conference on Small Satellites, Logan, Utah, USA, 1999
- [9] Reichbach, J.G, Sedwick, R.J. and Sanchez, M.M., "Micropropulsion System Selection for Precision Formation Flying Satellites", 37th AIAA/ASME/SAE/ASEE Joint Propulsion Conference and Exhibit, Salt Lake City, UT, AIAA-2001-3646, July, 2001
- [10] Osiander, R., Darrin, M.A.G and Champion, J.L., "MEMS and Microstructures In Aerospace Application", CRC Press, US, 2006
- [11] Micci, M.M and Ketsdever, A.D., "Micropropulsion for Small Spacecraft", Progress in Astronautics and Aeronautics, Volume 187, 2000
- [12] Grisnik, S.P and Smith, T.A., "Experimental Study of Low Reynolds Number Nozzles", NASA TM-89858, May 1987

- [13] Sellers, J.J., Paul, M. and Sweeting, M., "Investigation into Cost-Effective Propulsion System Option for Small Satellites," *Journal of Reducing Space Mission Cost*, Vol.1, pp.53-72, 1998
- [14] Myers, R.M. and Oleson, S.R., "Small Satellite Propulsion Option", *AIAA Journal*, pp.94-2997, 1994
- [15] Milligan, M.W., "Nozzle Characteristics in the Transition Regime between Continuum and Free Molecular Flow", *AIAA Journal*, Vol.2, No.6, 1964, pp. 1088-1092
- [16] Massier, P. F., Back, L. H., Noel, M. B., and Saheli, F., "Viscous Effects on the Flow Coefficient for a Supersonic Nozzle," *AIAA Journal*, Vol. 8, No. 3, March 1970, pp. 605-607
- [17] Kuluva, N.M. and Hosack, G.A., "Supersonic Nozzle Discharge at Low Reynolds Numbers", *AIAA Journal*, Vol.9, No.9, pp.1876-1879, 1971
- [18] Rothe, D.E., "Electro-Beam Studies of Viscous Flow in Supersonic Nozzles", *AIAA Journal*, Vol. 9, No.5, 1971, pp. 804-811
- [19] Murch, C., Broadwell, J., Silver, A. and Marvisz, T., "Low-Thrust Nozzle Performance", *AIAA Paper*, No.68-91, 1968
- [20] Whalen, M., "Low Reynolds Number Nozzle Flow Study", *NASA TM-100130*, 1987
- [21] Rae, W.J., "Some Numerical Results on Viscous Low-Density Nozzles Flows in the Slender Channel Approximation", *AIAA Journal*, Vol.9, No.5, 1971, pp. 811-920
- [22] Driscoll, R.J., "Study of the Boundary Layers in Chemical Laser Nozzles", *AIAA Journal*, Vol.14, No.11, pp.870-872, 1974
- [23] Chung, C.H., Kim, S.C., Stubbs, R.M. and DeWitt, K.J., "Low Density Nozzle Flow by Direct Simulation Monte Carlo and Continuum Methods", *Journal of Propulsion and Power*, Vol.11, pp.64-70, 1995
- [24] Hussaini, M.M. and Korte, J.J., "Investigation of Low-Reynolds-Number Rocket Nozzle Design Using PNS-Based Optimization Procedure", *NASA Technical Memorandum 110295*, 1996
- [25] Rao, G.V.R., "Exhaust Nozzle Contour for Maximum Thrust", *Jet Propulsion*, Vol.28, pp.377-382, 1958
- [26] Kim, S.C., "Calculations of low-Reynolds number Resistojet Nozzles", *Journal of Spacecraft and Rockets*, Vol.31, pp.256-264, 1994

- [27] Shimura, K., Asako, Yutaka. And Lee, J.H., “Numerical Analysis for Supersonic Flows in a Cooled Nozzle”, Numerical Heat Transfer, Part A: Applications: An International Journal of Computation and Methodology, Vol.26, Issue.6, 1994
- [28] Zelesnik, D., Micci, M. and Long, L., “Direct Simulation Monte Carlo Model of Low Reynolds Number Nozzle Flow”, Journal of Propulsion and Power, Vol.10, No.4, pp.546-553, 1994
- [29] Liang, S.M., Huang, K.L. and Chen, K.C., “Numerical Study of Low-Thrust Nozzles for Satellites”, Journal of Spacecraft and Rockets, Vol.33, No.5, 1996
- [30] Bayt, R.L and Breuer, K.L., “Viscous Effects in Supersonic MEMS-based Micronozzles” Proc. 3rd ASME Microfluids Symp, Anaheim, CA, 1998
- [31] Bayt, R.L and Breuer, K.L., “System Design and Performance of Hot and Cold Supersonic Microjets,” 39th AIAA Aerospace Sciences Meeting and Exhibit, Reno, Nevada, 2001
- [32] Reed, B.D., de Groot, W. and Dang, L., “Experimental Evaluation of Cold flow Micronozzles”, 37th AIAA/ASME/SAE/ASEE Joint Propulsion Conference 7 Exhibit, AIAA-2001-3521, Salt Lake City, UT, 2001
- [33] Ivanov, M., Markelov, G., Ketsdever, A., and Wadsworth, D., “Numerical Study of Cold Gas Micronozzle Flows,” AIAA Paper 99-0166, Jan. 1996.
- [34] Bird, G., “Molecular Gas Dynamics and the Direct Simulation of Gas Flows”, Clarendon Press, Oxford, 1994
- [35] Markelov, G.N. and Ivanov, M.S., “A Comparative Analysis of 2D/3D Micronozzle Flows by the DSMC Method”, 39th AIAA Aerospace Sciences Meeting & Exhibit, AIAA-2001-1009, Reno, NV, 2001
- [36] Markelov, G.N. and Ivanov, M.S., “Numerical Study of 2D/3D Micronozzle Flows”, Rarefied Gas Dynamics, 22nd International Symposium, 2001
- [37] Choudhuri, A.R., Baird B., Gollahalli, S.R. and Schneider, S.J., “Effects of Geometry and Ambient Pressure on Micronozzle Flow”, 37th AIAA/ASME/SAE/ASEE Joint Propulsion Conference and Exhibit, Salt Lake City, Utah, AIAA-2001-3331, 2001
- [38] Alexeenko, A.A., Levin, D.A., Gimelshein, S.F. and Collins, R.J., “Numerical Modeling of Axisymmetric and Three-Dimensional Flows in MEMS Nozzles”, 36th AIAA/ASME/SAE/ASEE Joint Propulsion Conference and Exhibit, Reston, VA, 2000
- [39] Alexeenko, A.A., Levin, D.A., Gimelshein, S.F., Collins, R.J. and Reed, B.D., “Numerical Modeling of Axisymmetric and Three-Dimensional Flows in

Microelectromechanical Systems Nozzles”, AIAA Journal, Vol.40, No.5, pp.897-904, 2002

- [40] Alexeenko, A.A., Levin, D.A., Collins, R.J. and Markelov, G.N., “Numerical Simulation of High Temperature Gas Flows in a Millimeter-Scale Thruster”, Journal of Thermophysics and Heat Transfer, Vol.16, No.1, pp.10-16, 2002
- [41] Alexeenko, A.A., Gimelshein, S.F., Levin, D.A., Ketsdever, A.D. and Ivanov, M.S., “Measurements and Simulation of Orifice Flow for Micropropulsion Testing”, Journal of Propulsion and Power, Vol.19, No.4, pp.588-594, 2003
- [42] Alexeenko, A.A., Levin, D.A., Fedosov, D.A., Gimelshein, S.F. and Collins, R.J., “Performance Analysis of Microthrusters Based on Coupled Thermal-Fluid Modeling and Simulation”, Journal of Propulsion and Power, Vol.21, No.1, pp.95-101, 2005
- [43] Alexeenko, A.A., Fedosov, D.A., Gimelshein, S.F., Levin, D.A. and Collins, R.J., “Transient Heat Transfer and Gas Flow in a MEMS-Based Thruster”, Journal of Microelectromechanical Systems, Vol.15, No.1, pp.181-194, 2006
- [44] Ketsdever, A.D., Clabough, M.T., Gimelshein, S.F. and Alexeenko, A.A., “Experimental and Numerical Determination of Micropropulsion Device Efficiencies at Low Reynolds Numbers”, AIAA Journal, Vol.43, No.3, pp.663-641, 2005
- [45] Louissos, W.F. and Hitt, D.L., “Viscous Effects in Supersonic Micro-Nozzles Flows: Transient Analysis”, 36th AIAA fluid Dynamics Conference and Exhibit, San Francisco, California, 2006
- [46] Louissos, W.F. and Hitt, D.L., “Heat Transfer & Viscous Effects in 2D & 3D Supersonic Micro-Nozzle Flows”, 37th AIAA fluid Dynamics Conference, Miami, Florida, 2007
- [47] Louissos, W.F. and Hitt, D.L., “Viscous Effects on Performance of Two-Dimensional Supersonic Linear Micronozzles”, Journal of Spacecraft and Rockets, Vol.45, No.4, 2008
- [48] Louissos, W.F. and Hitt, D.L., “Optimal Expansion Angle for Viscous Supersonic flow in 2-D Micro-Nozzles”, 35th AIAA Fluid Dynamics Conference and Exhibit, AIAA-2005-5032, Toronto, Ontario, 2005
- [49] Titov, E., Gallagher, R.A. and Levin, D., “Examination of a Collision-Limiter Direct Simulation Monte Carlo Method for Micropropulsion Applications”, Journal of Propulsion and Power, Vol.24, No.2, pp.311-321, 2008
- [50] Mo, H., Lin, C., Gokaltun, S. and Skudarnov, P.V., “Numerical Study of Axisymmetric Gas Flow in Conical Micronozzles by DSMC and Continuum Methods”, 44th AIAA Aerospace Sciences Meeting and Exhibit, AIAA-2006-991, 2006

- [51] Lin, C.X. and Gadepalli, V.V.V., “Navier-Stokes Modeling of Gas Flows in a De-Laval Micronozzle”, 44th AIAA Aerospace Sciences Meeting and Exhibit, AIAA-2006-1425, 2006
- [52] Lin, C.X. and Gadepalli, V.V.V., “A Computational Study of Gas Flow in a De-Laval Micronozzle at Different Throat Diameters”, International Journal for Numerical Methods in Fluids, Vol.59, pp.1203-1216, 2008
- [53] Ahmad, R.A., “Discharge Coefficients and Heat Transfer for Axisymmetric Supersonic Nozzles”, Heat Transfer Engineering, Vol.22, pp.40-61, 2001
- [54] Bruccoleri, A.R. and Lozano, P., “Experimental Analysis of Low Reynolds Number Supersonic Flow Efficiency”, 45th AIAA/ASME/SAE/ASEE Joint Propulsion Conference and Exhibit, Denver, Colorado, 2009
- [55] Bruccoleri, A.R., Leiter, R., Drela, M. and Lozano, P., “Experimental Effects of Nozzle Geometry on Flow Efficiency at Low Reynolds Numbers”, Journal of Propulsion and Power, Vol.28, No.1, 2012
- [56] Zhang, W.M., Meng, G. and Wei, X., “A Review on Slip Models for Gas Microflows”, Microfluidics and Nanofluidics, ISSN 1613-4982, DOI 10.1007/s10404-012-1012-9
- [57] Ho, C.M. and Tai, Y.C., “Micro-Electro-Mechanical-Systems (MEMS) and Fluid Flows”, Annual Review of Fluid Mechanics, Vol.30, 99.579-612, 1998
- [58] Maxwell, J.C., “On Stresses in Rarefied Gases Arising from Inequalities of Temperature”, Philosophical Transactions of the Royal Society Part 1, Vol.170, pp.231-256, 1879
- [59] Smoluchowski, von M., “Ueber Wärmeleitung in verdünnten Gasen”, Annalen der Physik und Chemi, Vol.64, pp.101-130, 1898
- [60] Karniadakis, George, Beskok, Ali, Ali, Aluru and Narayan., “Microflows and Nanoflows Fundamentals and Simulation ”, Interdisciplinary Applied Mathematics, Vol.29, Springer Science + Business Media, Inc., New York, 2005
- [61] Piekos, E.S. and Breuer, K.S., “DSMC Modeling of Micromechanical Devices”, 30th AIAA Thermophysics Conference, San Diego, CA, June, 1995
- [62] Piekos, E.S. and Breuer, K.S., “Numerical Modeling of Micro-Mechanical Devices using the Direct Simulation Monte Carlo Method”, Journal of Fluids Engineering, Vol.118, pp.464-469, 1996

- [63] Nance, R.P., Hash, D.B. and Hassan, H.A., "Role of Boundary Conditions in Monte Carlo Simulation of MEMS Devices", *Journal of Thermalphys and Heat Transfer*, Vol.12, pp.447-449, 1998
- [64] Liou, W.W. and Fang, Y., "Implicit Boundary Conditions for Direct Simulation Monte Carlo Method in MEMS Flow Predictions", *Computer Modeling in Engineering and Sciences*, Vol.4, pp.119-128, 2000
- [65] Wang, M.R. and Li, Z.X., "Numerical Simulations on Performance of MEMS-based Nozzles at Moderate or Low Temperatures", *Microfluidics Nanofluidics*, Vol.1, pp.62-70, 2004
- [66] Shen, C., "Rarefied Gas Dynamics, Fundamentals, Simulation and Micro Flows", Springer, Berlin Heidelberg, New York, 2005
- [67] Raju, R., Pandey, B.P. and Roy, S., "Finite Element Model of Fluid Flow Inside a Microthruster", *NanoTech 2002 Conference*, AIAA-2002-5733, 2002
- [68] Rossi, C., Rouhani, M.D. and Esteve, D., "Prediction of the Performance of a Si-Micromachined Microthruster by Computing the Subsonic Gas Flow inside the Thruster", *Sensors and Actuators, Physical A*, Vol.87, pp.96-104, 2000
- [69] Rossi, C., Esteve, D., Fabre, N., Do Conto, T. and Conedera, V., "New Generation of MEMS-Based Microthruster for Microspacecrafts Applications" *Conference on Micro & Nano Technologies for Space Applications*, Pasadena, CA, April 1999
- [70] Boyd, I.D., Penko, P.F., Meissner, D.L. and Dewitt, K.J., "Experimental and Numerical Investigations of Low-Density nozzle and Plume Flows of Nitrogen", *AIAA Journal*, Vol.30, No.10, 1992
- [71] Boyd, I.D., Jafry, Y. and Beukel, J.V., "Particle Simulation of Helium Microthruster flows", *Journal of Spacecraft and Rockets*, Vol.31, No.2, pp.217-277, 1994
- [72] Boyd, I.D. and VanGilder, D.B., "Computational and Experimental Investigations of Rarefied Flows in Small Nozzles", *AIAA Journal*, Vol.34, No.11, 1996
- [73] Boyd, I.D., "Monte Carlo Simulation of Nonequilibrium Flow in a Low-Power Hydrogen Arcjet", *Physics of Fluids*, Vol.9, No.10, pp.3086-3095, 1997
- [74] We, J.S. and Tseng, K.C., "Analysis of Micro-Scale Gas Flows with Pressure Boundaries Using Direct Simulation Monte Carlo Method", *Computer & Fluids*, Vol.30, pp.711-735, 2001

- [75] Lockerby, D.A., Reese, J.M., Emerson, D.R. and Barber, R.W., “Velocity Boundary Condition at Solid Walls in Rarefied Gas Calculations”, *Physical Review E* 70, 017303, 2004
- [76] Hao, P.F., Ding, Y.T., Yao, Z.H., He, F. and Zhu, K.Q., “Size Effects on Gas Flow in Micro Nozzles”, *Journal of Micromechanics and Microengineering*, Vol.15m pp.2069-2073, 2005
- [77] Xie, C., Shen, C. and Fan, J., “Statistical Simulation of Rarefied Gas Flows in Micro-Channels”, *Journal of Computational Physics*, Vol.189, pp.512-526, 2003
- [78] Xie, C., Fan, J. and Shen, C., “Statistical Simulation of Rarefied Gas Flow in Micro-Channels”, 23rd Rarefied Gas Dynamics, AIP, New York, 200
- [79] Xie, C., “Subsonic Choked Flow in Micro-Channel”, *Physics of Fluids* 18, 127104 (2006)
- [80] Xie, C., “Characteristics of Micronozzle Gas Flows”, *Physics of Fluids* 19, 037102 (2007)
- [81] Li, X.H., Yu, X.M., Zhang, D.C., Cui, H.H., Li, T., Wang, Y. and Wang, Y.Y., “Characteristics of Gas Flow within a Micro Diffuser/Nozzle Pump”, *China Physics Letters*, Vol.23, No.5, 2006
- [82] Xu, J. and Zhao, C., “Two-Dimensional Numerical Simulations of Shock Waves in Micro Convergent-Divergent Nozzles”, *International Journal of Heat and Mass Transfer*, 50 (2007) 2434-2438
- [83] Morinigo, J.A., Quesada, J.H. and Requena, F.C., “Slip-Model Performance for Underexpanded Micro-scale Rocket Nozzle Flows”, *Journal of Thermal Science*, Vol.16, No.3, pp.223-230, 2007
- [84] Morinigo, J.A., Quesada, J.H. and Requena, F.C., “Underexpanded Micro-nozzle Flow Simulation with Coupled Thermal-Fluid Modeling”, *Thermal, Mechanical and Multi-Physics Simulation Experiments in Microelectronics and Micro-Systems International Conference*, 2007
- [85] Morinigo, J.A. and Quesada, J.H., “Solid-Gas Surface Effect on the Performance of a MEMS-class Nozzle for Micropropulsion”, *Sensors and Actuators A: Physical*, 162 (2010) 61-71
- [86] Liu, M., Zhang, X., Zhang, G and Chen, Y., “Study on Micronozzle Flow and Propulsion Performance using DSMC and Continuum Methods”, *Acta Mechanica Sinica*, Vol.22, No.5, pp.409-416, 2006

- [87] Broc, A., Benedictis, S.D., Dilecce, G., Viglotti, M., Sharafutdinov, R.G. and Skovorodko, P.A., “Experimental and Numerical Investigation of an O₂/NO Supersonic Free Jet Expansion”, *Journal of Fluid Mechanics*, 500, 211, 2004
- [88] Jamison, A.D. and Ketsdever, A.D., “Low Reynolds Number Performance of an Underexpanded Orifice and a Delaval Nozzle”, *23rd Rarefied Gas Dynamics*, AIP, New York, 2003
- [89] Wadsworth, D.C. and Erwin, D.A., “Two-dimensional Hybrid Continuum/Particle Approach for Rarefied Flows”, *AIAA 23rd Plasmadynamics & Lasers Conference*, AIAA-92-2975, Nashville, TN, July, 1992
- [90] Vashchenkov, P.V., Kudryavtsev, A.N., Khotyanovsky, D.V. and Ivanov M.S., “DSMC and Navier-Stokes Study of Backflow for Nozzle Plumes Expanding into Vacuum”, In *Processing 24th Rarefied Gas Dynamics International Symposium*. AIP Conference Processing, Vol.762, 2005
- [91] Tiwari, S., Klar, A. and Hardt, S., “A Particle-Particle Hybrid Method for Kinetic and Continuum Equations”, *Journal of Computational Physics*, 61:1273-98, 2009
- [92] Wu, J.S., Lian, Y.Y., Cheng, G., Koomullil, R.P. and Tseng, K.C., “Development and Verification of a Coupled DSMC-NS Scheme using Unstructured Mesh”, *Journal of Computational Physics*, 219:579-607, 2006
- [93] Torre, La.F., Kenjeres, S., Kleijin, C.R. and Moerel, J.L.P.A., “Evaluation of Micronozzle Performance through DSMC, Navier-Stokes and Coupled DSMC/Navier-Stokes Approaches”, *Lecture Notes in Computer Science*, Vol.5544, Los Angeles, Springer, 2009
- [94] Torre, F.La., Kenjeres, S., Moerel, J.L. and Kleijn, C.R., “Hybrid Simulations of Rarefied Supersonic Gas Flows in Micro-Nozzles”, *Computers & Fluids*, Vol.49, pp.312-322, 2011
- [95] McGhee, R.J., “Some Effects of Jet Pluming on the Static Stability of Ballistic Bodies at a Mach Number of 6.00”, *NASA TN D-3698*, 1966
- [96] McGhee, R. J., “Jet-Plume-Induced Flow Separation of Axisymmetric Bodies at Mach Number of 3.00, 4.50 and 6.00”, *NASA TM X-2059*, 1970
- [97] Walitt, L., Wilcox, D.C. and Liu, C.Y., “Numerical Study of Plume-Induced Flow Separation”, *Computers and Fluids*, Vol.3, pp.235-255, 1975
- [98] Henderson, J.H., “An Investigation for Modeling Jet Plume Effects on Missile Aerodynamics”, *U.S Army Missile Command, Technical Report RD-CR 82-25*, July, 1982

- [99] Chatelain, A. and Hadjadj, A., “Computational Study of a Plume Induced Flow Separation on a Boat-Tailed Afterbody”, 4th Symposium on Aerothermodynamics for Space Vehicles, Capua, Italy, ESA SP 487, 2002
- [100] Ebrahimi, H., “Numerical Investigation of Twin-Nozzle Rocket Plume Phenomenology, Part II”, 36th Aerospace Sciences Meeting and Exhibit, January 12-15, Reno, NV, 1998
- [101] Bannink, W.J., Houtman, E.M. and Bakker, P.G., “Base Flow/Underexpanded Exhaust Plume Interaction in a Supersonic External Flow”, 8th AIAA International Space Planes and Hypersonic Systems and Technologies Conference, Norfolk, VA, 1998
- [102] Matesanz, A. and Velazquez, A., “Numerical Simulation of Base-Flow/Plume Interaction”, 8th AIAA International Space Planes and Hypersonic Systems and Technologies Conference, 1998
- [103] Raghunathan, S., Kim, H. D. and Benard, E., “Plume Interference Effects on Missile Bodies”, 39th Aerospace Sciences Meetings and Exhibit, January 8-11, Reno, NV, 2001
- [104] Bakker, P.G., Bannink, W.J., Serval, P. and Reijasse, Ph., “CFD Validation for Base Flows with and without Plume Interaction”, AIAA Paper 2002-0438, Jan, 2002
- [105] Lee, Y.K., Raghunathan, S. and Benard, E., “Plume Interference Effect on Missile Bodies and Control”, 41st Aerospace Sciences Meeting and Exhibit, January 2003, Reno, NV, 2003
- [106] Van Oudheusden, B.W. and Scarano, F., “PIV Investigation of Supersonic Base-Flow-Plume Interaction”, Particle Image Velocimetry, Topics in Applied Physics, Vol.112, pp.465-474, 2008
- [107] Kim, J.G., Lee, J.W., Choi, J.K. and Kim, K.H., “Investigation on the Characteristics of Plume Induced Flow Separation and Wall Heat Transfer”, 49th AIAA Aerospace Sciences Meeting Including the New Horizons Forum and Aerospace Exposition, January, Orlando, FL, 2011
- [108] Kim, J.G., Lee, J.W. and Kim, K.H., “Investigation on the Characteristics of Plume Induced Flow Separation and Wall Heat Transfer”, Journal of Spacecraft and Rockets, Vol.49, No.1, 2012
- [109] Gusman, M. and Housman, J., “Best Practices for CFD Simulations of Launch Vehicle Ascent with Plumes—OVERFLOW Perspective”, 49th AIAA Aerospace Sciences Meeting, January, Orlando, FL, 2011

- [110] Deere, K., Elmiligui, A. and Hamid, K.S.A., "USM3D Simulations of Saturn V Plume-Induced Flow Separation", *Journal of Spacecraft and Rockets*, Vol.49, No.4, 2012
- [111] Ebrahimi, H.B., "CFD Validation and Evaluation for Reacting Flows, Part III", 33rd Aerospace Sciences Meeting and Exhibit, January, Reno, NV, 1995
- [112] Ebrahimi, H.B., Levine, J. and Kawasaki, A., "Numerical Investigation of Twin-Nozzle Rocket Plume Phenomenology", 35th Aerospace Sciences Meeting and Exhibit, January 6-10, Reno, NV, 1997
- [113] Burt, M.J. and Boyd, I.D., "High Altitude Plume Simulation for a Solid Propellant Rocket", 45th AIAA Aerospace Sciences Meeting and Exhibit, January, Reno, NV, 2007
- [114] Lee, J.W., Kim, J.G. and Kim, K.H., "Effects of AL_2O_3 Particle on Convective and Radiative Heat Flux to Rocket Base Surface", 7th International Conference on Computational Fluid Dynamics, July, Big Island, HA, 2012
- [115] Hall, L., Applebaum, M.P. and Eppard, W.M., "Multi-Species Effects for Plume Modeling on Launch Vehicle Systems", 49th AIAA Aerospace Sciences Meeting including the New Horizons Forum and Aerospace Exposition, January, Orlando, FL, 2011
- [116] Applebaum, M.P., Eppard, W.M. and Hall, L., "Multi-Species Effects for Plume Modeling on Launch Vehicle Systems", *Journal of Spacecraft and Rockets*, Vol.49, No.5, 2012
- [117] Wright, M.J., Rao, R.M., Candler, G.V., Hong, J.S., Schilling, T.A. and Levin, D.A., "Modeling Issues in the Computation of Plume Radiation Signatures", AIAA Paper, No.98-3622, 1998
- [118] Rao, R.M., Sinha, K., Candler, G.V., Wright, M.J. and Levin, D.A., "Numerical Simulations of Atlas II Rocket Motor Plumes", 39th AIAA Aerospace Sciences Meeting and Exhibit, January, Reno, NV, 2001
- [119] Alexeenko, A.A., Gimelshein, N.E., Levin, D.A., Gimelshein, S.F., Hong, J.S., Schilling, T., Collins, R.J., Rao, R. and Candler, G., "Modeling of Radiation in the Atlas Plume-Flow", 39th AIAA Aerospace Sciences Meeting and Exhibit, January, Reno, NV, 2001
- [120] Alexeenko, A.A., Gimelshein, N.E., Levin, D.A., Gimelshein, S.F., Hong, J.S., Schilling, T., Collins, R.J., Rao, R. and Candler, G., "Modeling of Radiation in the Atlas Plume", *Journal of Thermophysics and Heat Transfer*, Vol.16, No.1, 2002

- [121]Futron Corporation, "Space Transportation Costs: Trends in Price per Pound to Orbit 1990-2000," 2002 pp. 1-8, www.futron.com
- [122]Gao, Y. and Baker, J., "Surface Modification on Supersonic Micronozzle Flow Behavior", Journal of Propulsion and Power, 2014
- [123]Lanzafame, R. and Messian M., "A New Method for the Calculation of Gases Enthalpy", Energy Conversion Engineering Conference and Exhibit, (IECEC) 35th Intersociety, Vol.1, pp.318-328, July, 2000
- [124]White, F.M., "Viscous Fluid Flow", McGraw-Hill, Inc., New York, 2nd edition, 1991
- [125]Menter, F.R., "Two-Equation Eddy-Viscosity Turbulence Models for Engineering Applications", AIAA Journal, Vol.32, No.8, pp.1598-1605, August, 1994
- [126]Bardian, J.E., Huang, P.G. and Coakly, T.J., "Turbulence Modeling Validation, Testing and Development", NASATM-110446, 1997
- [127]Hoffmann, K.A and Chiang, S.T., "Computational Fluid Dynamics", Engineering Education System, Wichita, KS, USA, 2000
- [128]Courant, R., Isaacson, E and Rees, M., "On the Solution of Nonlinear Hyperbolic Differential Equations by Finite Difference", Pure and Applied Mathematics, Vol.5, No.3, pp.243-255, 1952
- [129]Bayt, R. L., "Analysis, Fabrication and Testing of a MEMS-based Micropropulsion System", Ph.D. Dissertation, Massachusetts Institution of Technology, Department of Aeronautics and Astronautics, Cambridge, May 1999
- [130]Anderson, J.D., "Modern Compressible Flow with Historical Perspective", McGraw-Hill Companies, Inc., 3rd Edition, New York, 1975
- [131]Yakhot, V., Orszag, S.A., Thangam, S., Gatski, T.B. and Speziale, C.G., "Development of Turbulence Models for Shear Flows by a Double Expansion Technique", Physics of Fluids A, Vol.4, No.7, pp.1510-1520, 1992
- [132]Giancoli, D., "Physics Principles with Applications", University of California, Berkeley, 6th Edition
- [133]Flanga, R.A., Hinson, W.F. and Crawford, D.H., "Exploratory Tests on the Effects of Jet Plumes on the Flow over Cone-Cylinder-Flare-Bodies", NASA TN D-1000, 1962
- [134]Nyberg, S.E. and Agrell, J., "Investigation of Modeling Concepts for Plume-Afterbody Flow Interactions", AERONAUTICAL RESEARCH INST OF SWEDEN STOCKHOLM, No. FFA-TN-AU-1384, 1981